Chemical Engineering Journal 466 (2023) 143225

Contents lists available at ScienceDirect

Chemical Engineering Journal

journal homepage: www.elsevier.com/locate/cej

Robotic platform for accelerating the high-throughput study of silver nanocrystals in sensitive/selective Hg^{2+} detection

Lixiang Xing [a,b], Zijian Chen [b], Wei Chen [b], Paul K. Chu [c], Xue-Feng Yu [a,b,d,*], Haitao Zhao [a,b,*]

[a] Shenzhen Key Laboratory of Micro/Nano Biosensing, Shenzhen Institute of Advanced Technology, Chinese Academy of Sciences, Shenzhen, Guangdong 518055, PR China
[b] Materials Interfaces Center, Shenzhen Institute of Advanced Technology, Chinese Academy of Sciences, Shenzhen 518055, Guangdong, PR China
[c] Department of Physics, Department of Materials Science and Engineering, and Department of Biomedical Engineering, City University of Hong Kong, Tat Chee Avenue, Kowloon, Hong Kong, China
[d] Hubei Three Gorges Laboratory, Yichang, Hubei 443007, PR China

ARTICLE INFO

Keywords:
Mercury ion detection
Controllable synthesis
High-throughput study
Machine learning
Silver nanocrystals

ABSTRACT

Colorimetric determination of trace mercury ions (Hg^{2+}) with high reproducibility and sensitivity is urgently required for water safety and environmental monitoring. Herein, an automated robotic platform is described for high-throughput and controllable synthesis of colloidal silver nanocrystals (Ag NCs) and sensitive/selective colorimetric determination of Hg^{2+} in aqueous solutions. The predicted models of optical simulation are constructed as data-driven models to evaluate the quality of Ag NCs synthesized by a wet-chemical method. Based on an experimental database derived by optical characterization, the machine-learning (ML) model which covers multiple synthesis parameters is established for uniform synthesis of Ag NCs with controllable sizes matching the classical growth model. Moreover, the database of more than 1,200 valid samples established for the optical properties of Ag NCs is digitized to correlate with their average size. Optimized manual re-synthesis of high-quality Ag NCs demonstrates the practical feasibility and scalability of established models. The prepared Ag NCs can be used directly or modified with polymer ligands for quantitative detection of Hg^{2+} in the linear range from 0.01 to 200 μM with a detection limit of 3 nM. The strategy provides a scientific and effective way for the high-throughput study of nanoscale optical materials in chemical engineering and environmental monitoring.

1. Introduction

Mercury (Hg^{2+}) is one of the common and toxic heavy metal ions in wastewater causing health hazards and environmental safety concerns [1–3]. The safety level of Hg^{2+} in drinking water is 10 nM as stipulated by the U.S. Environmental Protection Agency [4,5], and sensitive and accurate detection of Hg^{2+} in aqueous media is thus imperative. Compared to common analytical techniques such as atomic adsorption spectroscopy (AAS), atomic fluorescence spectroscopy (AFS), and inductively-coupled plasma emission spectroscopy (ICP-ES) [6–8], colorimetric determination of Hg^{2+} based on surface plasmon resonance (SPR) offers advantages such as low cost and simple operation [3,9,10]. However, plasmonic nanomaterials for colorimetric detection usually have poor reproducibility and low sensitivity because of the uniform optical phenomenon and therefore, it is crucial to develop a technique capable of controllable synthesis of stable nanomaterials with high SPR efficiency for colorimetric determination of Hg^{2+}.

Silver nanocrystals (Ag NCs) are desirable optical sensing materials due to their excellent SPR efficiency [11,12] and efforts have been made for controllable synthesis of stable Ag NCs with tailored optical properties by wet-chemical methods [13–17]. However, the number of valid samples in most databases is too small for universal application. In general, metal precursors, stabilizing agents, shape-control agents, reducing agents, and other supplementary agents are required for the wet-chemical synthesis of NCs [18–21], and their roles become very complex when multiple parameters must be optimized at the same time. Obviously, it is not scientific to simply summarize some recipes without a comprehensive consideration of the impact of different parameters. In addition, synthetic agents with low molecular weights are more favorable to optical sensors from the perspective of surface activity [22,23].

* Corresponding authors at: Shenzhen Key Laboratory of Micro/Nano Biosensing, Shenzhen Institute of Advanced Technology, Chinese Academy of Sciences, Shenzhen, Guangdong 518055, PR China.
E-mail addresses: xf.yu@siat.ac.cn (X.-F. Yu), ht.zhao@siat.ac.cn (H. Zhao).

https://doi.org/10.1016/j.cej.2023.143225
Received 9 February 2023; Received in revised form 21 April 2023; Accepted 25 April 2023
Available online 28 April 2023
1385-8947/

Hence, it is necessary to develop a high-throughput technique for controllable synthesis encompassing multiple parameters.

One way to realize this goal is to enhance big data acquisition and processing by artificial intelligence (AI) [24,25]. Recently, technological advances in modular robotic systems have spurred the development of chemical automation [26–29] as a powerful and high-throughput tool for screening synthetic strategies and recipes due to the high efficiency, less manpower, and high accuracy. Although some automated platforms focusing on organic synthesis in chemical engineering have been reported [30–33], there have been few reports about robotic platforms pertaining to the synthesis and characterization of inorganic nanomaterials. Meanwhile, the lack of proper descriptors for multi-parameter synthesis has become a bottleneck restricting the high-throughput study [34,35]. Databases with complex features can be iteratively established with advanced machine learning (ML) algorithms [36–39] and correlation analysis can be accelerated with a better understanding of the relationship between material properties and synthesis parameters [40–42]. The strategy combining automated platforms and ML algorithms may pave the way for the high-throughput study of Ag NCs.

Herein, we report a robotic platform for the high-throughput study of colloidal Ag NCs for Hg^{2+} detection (Fig. 1). Spectral analyses of desirable spherical Ag NCs are carried out based on optical simulation (Fig. 1A) and then adopted as data-driven models with ML (Fig. 1B) to evaluate the quality of Ag NCs synthesized by the robotic platform (Fig. 1C). The relationship between multiple synthesis parameters is explored and clarified by automated optical characterization (Fig. 1D) to establish robust databases with ML models for controllable synthesis and optical properties of Ag NCs (Fig. 1E). The practicality of established models is investigated by scale-up exploration and comparative manual synthesis (Fig. 1F). The Ag NCs are utilized as optical sensors for visual colorimetric detection of Hg^{2+} to evaluate the reproducibility and sensitivity (Fig. 1G).

2. Materials and methods

2.1. Optical simulation based on Mie theory

The optical efficiency of Ag NCs was derived by Mie theory [43,44], which was widely used to simulate light scattering. Extinction efficiencies of spherical Ag NCs dispersed in water at different wavelengths were calculated and the average diameters (D, 30–220 nm) and standard deviations (SD, 2–40 %) of Ag NCs with a normal distribution were set by statistical calculations of 50 discrete values. The refractive indexes of silver and water at different wavelengths were basic parameters in the simulation (Fig. S1, Supporting Information). The theoretical simulation yielded standard optical parameters (Table S1) under ideal conditions to guide the data screening.

2.2. Synthesis of Ag NCs

The Ag NCs were synthesized by the robotic platform (Fig. S2) based on one-pot seeded growth recipes (Table S2 to S6). Firstly, the aqueous solutions of silver nitrate ($AgNO_3$), trisodium citrate (TSC), ammonia water ($NH_3{\cdot}H_2O$, 0.93 %), ascorbic acid (AA), and Ag-NC seeds [45] (Fig. S3) were prepared manually and placed at suitable positions of the pipetting module for automated synthesis of Ag NCs. As an example, in the synthesis of 50 nm Ag NCs, the seed solution (249 μL, 4.26×10^{11} mL^{-1}), $AgNO_3$ solution (80 μL, 5 mM), TSC solution (40 μL, 5 mM), and $NH_3{\cdot}H_2O$ solution (180 μL, 500 mM) were pipetted successively into water (151 μL) in a 96-well microplate which was then placed and

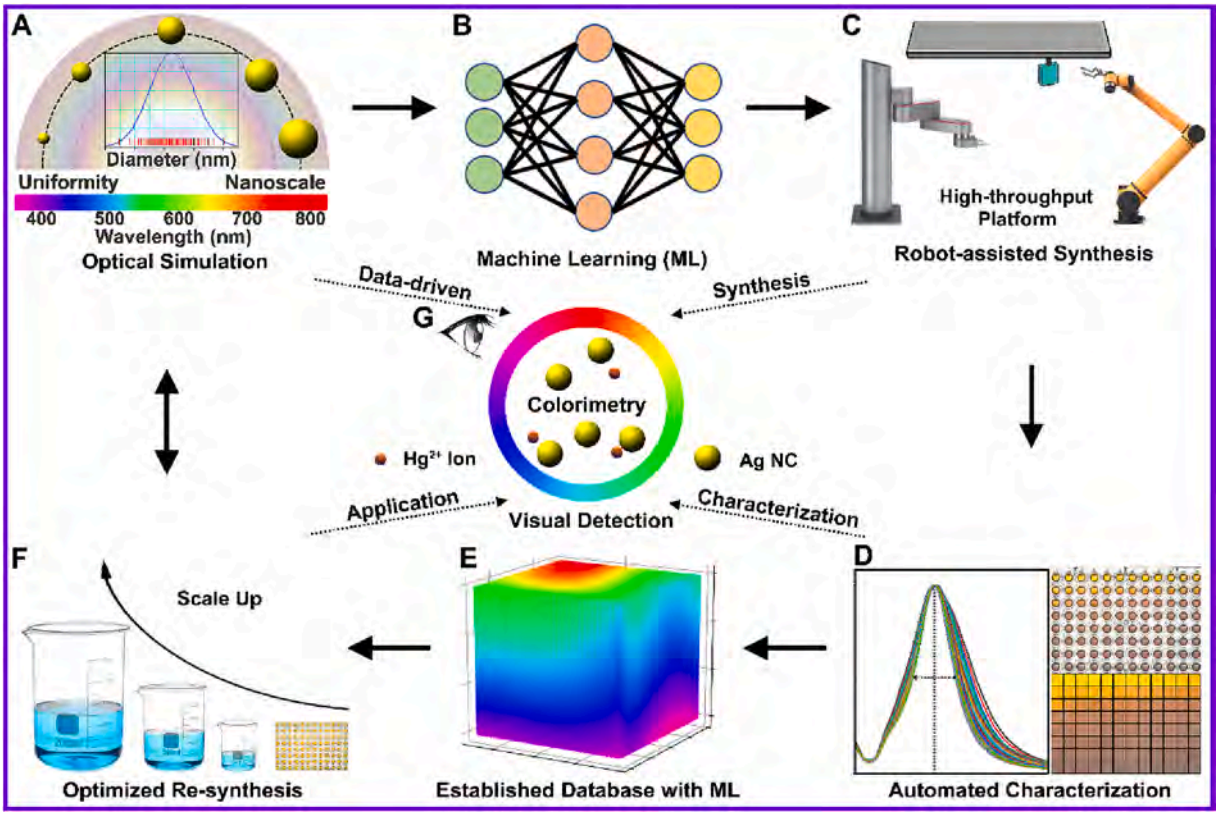

Fig. 1. Schematic illustration of the high-throughput study of Ag NCs for Hg^{2+} detection. (A) Optical simulation by Mie theory to predict the uniformity and nanoscale of spherical Ag NCs. (B) Machine learning to contrive data-driven models to evaluate the size distribution and average size of Ag NCs from spectra. (C) Robot-assisted synthesis of colloidal Ag NCs using the high-throughput automated platform. (D) Automated optical characterization including extinction spectra, high-quality digital photos, and RGB color-block photos. (E) Established database by ML model for Ag NCs including synthesis parameters and optical properties. (F) Optimized re-synthesis of Ag NCs beyond this platform through scale-up exploration. (G) Visual colorimetric detection of Hg^{2+} by Ag NCs.

stirred on the shaker to mix completely. The mixture on the microreactor was finally placed on the shaker for 20 min to complete the growth of Ag NCs after the last injection of AA solution (300 μL, 2 mM). The total volume of the final mixture was 1 mL and up to 96 experiments could be completed in one batch on the 96-well microreactor with automated pipettes. In the synthetic reaction, the mobile robot and six-axis robotic arm automatically transported the microplate to designated positions on the platform to perform predesigned operations including pipetting, shaking, data acquisition, storage, etc.

2.3. Scaling up of synthesis

The scale-up experiments were carried out by volume expansion based on the recipes extracted from established databases (Table S5 and S6). The volumes of 1 mL, 2 mL, and 5 mL were operated in microplates on the automated platform, while the volumes of 10 mL, 50 mL, 300 mL, and 1000 mL were operated in glass beakers manually not using the platform. For mass production of Ag NCs, the synthesis process was the same as mentioned above and the synthesis parameters in different volumes were strictly controlled in accordance with the recipes shown by established databases and models.

2.4. Optical characterization

After the synthesis, optical characterization was carried out *in situ* on the automated platform. The microplate was taken out from the shaker and 200 μL of the dispersion was transferred from each well to a new transparent microplate for colorimetric and spectroscopic analysis using the robotic platform. High-resolution images were acquired from the Ag-NC dispersions by a camera and the RGB color-block photos were converted and generated from the corresponding images for digital analysis. UV–Vis spectrophotometry was performed on the spectrum (Thermo Multiskan Skyhigh) in the range between 300 nm and 1,000 nm at steps of 1 nm. The key information was extracted from extinction spectra and RGB photos.

2.5. Visual detection of Hg^{2+}

Different metal ions including Na^{+}, K^{+}, Li^{+}, Mg^{2+}, Ca^{2+}, Zn^{2+}, Al^{3+}, Fe^{2+}, Fe^{3+}, Co^{2+}, Ni^{2+}, Ti^{4+}, Cu^{2+}, Cd^{2+}, Cr^{3+}, Mn^{2+}, Sr^{2+}, Zr^{4+}, Ag^{+}, Ba^{2+}, Pb^{2+}, Ga^{3+}, and Hg^{2+} (0.2 mM) were determined by the 50 nm Ag NCs optically using the robotic platform. The aqueous solutions containing various metal ions (100 μL) were pipetted into the aqueous solution of Ag NCs (900 μL) on the microplate, placed on the shaker, and stirred vigorously for 5 min at room temperature. The control (blank) experiment was conducted with deionized water. The color change and extinction spectra of aqueous solutions were analyzed in comparison.

To determine the concentration of Hg^{2+}, three types of Ag NCs modified with TSC, polyvinyl pyrrolidone (PVP), and gelatin (GEL) ligands were used. A series of aqueous solutions with different standard concentrations of Hg^{2+} were prepared and determined by the aforementioned method. The standard curves were obtained by plotting the changing ratios ($\Delta E/E_{max}$) of extinction intensities with the Hg^{2+} concentrations. The relevant detection limits were calculated according to the equation of $3S_b/m$ [5,16], where S_b and m are the standard deviation of blank signals and the slope of fitting curves, respectively.

The practicability pertaining to Hg^{2+} detection was verified with the aid of multiple actual samples. The real water samples were obtained from the Dasha River in Shenzhen and treated by a 0.22 mm membrane filter after physical precipitation. These real samples were spiked with standard concentrations of Hg^{2+} and then mixed with the solutions of Ag NCs for colorimetric analysis. As mentioned above, the real samples containing Hg^{2+} were subjected to the test, and Hg^{2+} concentrations were calculated by the changing ratios of peak intensities and established linear curves. All tests were carried out three times to confirm the reproducibility.

2.6. Machine learning

Linear regression and logistic regression were two widely used and effective ML algorithms [46] for analyzing the results of optical simulations, simple single-factor synthesis, and quantitative detection. These algorithms maintained the interpretability of original features and established receptive models for applications. As an advanced ML algorithm, the sure independence screening and sparsifying operator (SISSO) was a supervised approach to identify important features in a given feature space [39,47], which was used to describe the nature or function of a complex target (herein multiple synthesis parameters and color GRB data). The feature space was generated iteratively by a series of algebraic and functional operators and over 33,000 features were included in our case. The challenge of determining the best sparse solution was solved by SISSO which prescreened the optimized sub-space of the vast feature space and then determined the optimized solution.

3. Results and discussion

3.1. Controllable synthesis of Ag NCs

The extinction spectra of different spherical Ag NCs dispersed in water are simulated theoretically (Fig. S1) and then ML-predicted models are implemented to evaluate the quality of Ag NCs synthesized by the robotic platform (Fig. 2). The use of big data analysis to determine optical efficiency has become popular in materials informatics [24,48]. The calculated extinction spectra of Ag NCs with different size distributions (SD, 2–40 %) are shown in Fig. 2A and the average size of Ag NCs is fixed at 60 nm. The uniformity of Ag NCs is better for a smaller full-width at half-maxima (FWHM) of extinction peak, while the peak position shows no large change (Table S1). The ML-predicted model of the size and FWHM ($R^2 = 0.999$, Fig. 2B) is established with logistic regression and further used to guide data screening in the uniform synthesis. The SD of Ag NCs is less than 10 % if the FWHM of extinction peak is less than 73 nm reflecting the production of high-quality Ag NCs.

TSC, $NH_3{\cdot}H_2O$, and AA are selected as stabilizing agents [18], shape-control agents [14], and reducing agents [15] for green synthesis without high polymers, respectively. The amounts of Ag precursors (including seeds and $AgNO_3$) are fixed to make the average size of Ag NCs to be about 60 nm. High-throughput synthesis of Ag NCs (Table S2 to S4) is carried out on the automated platform to establish the experimental database. It can meet the demands of wet-chemical synthesis and optical characterization by incorporating various components on the robotic platform (Fig. S2). In the single-factor experiments (Fig. S4 and S5), the concentrations of different agents affect the uniformity (FWHM) of Ag NCs and should be adjusted. The double-factor and triple-factor experiments are carried out to investigate the synergies between various agents (Fig. S6 to S10). Accordingly, the 1D curves derived from single-factor experiments are extended into ML models encompassing 2D surfaces and 3D space visually in the multiple-factor experiments. The interactions between multiple synthesis parameters can be observed intuitively and the optimal conditions are predicted to demonstrate the broad scope of recipes for homogeneous growth of Ag NCs (red zone in the model, Fig. 2C). The experimental results are in good agreement with the results predicted by the model (Table S7), thus demonstrating that the training model based on the experimental database (Fig. S11) can be applied to uniform and controllable synthesis of Ag NCs. Moreover, the thermo-kinetic analysis (Fig. S12 and S13) reveals that ammonia plays a vital role in regulating the redox potentials as well as growth rates.

The calculated extinction spectra of Ag NCs with different average sizes (SD = 10 %) are shown in Fig. 2D. The SPR peaks redshift to a longer wavelength with a larger size (Table S1). Similarly, the ML-predicted model of the average size and dipolar peak position is established by fitting ($R^2 = 0.999$, Fig. 2E) to guide data screening and control the size of Ag NCs. Based on the optimal conditions given by the

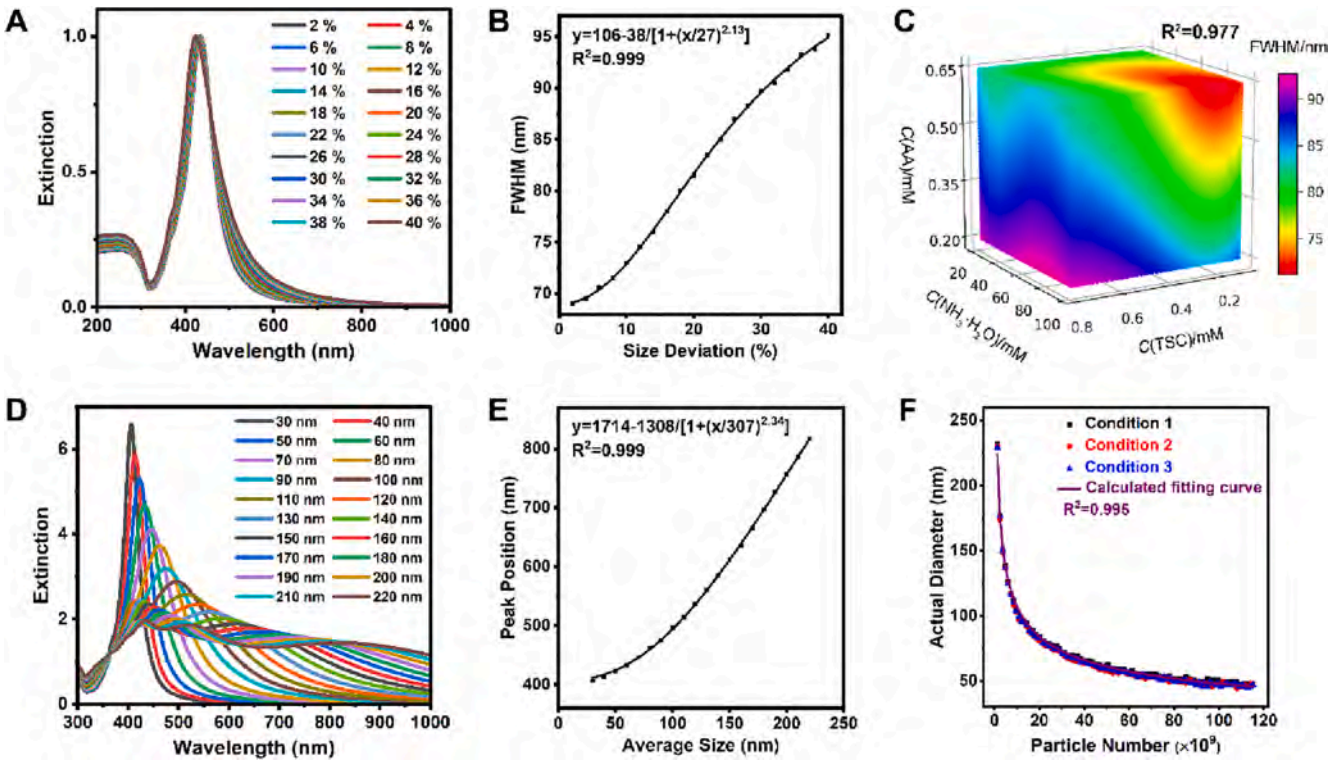

Fig. 2. High-throughput study of Ag NCs for controllable synthesis. (A) Calculated extinction spectra of 60 nm Ag NCs with different size distributions (SD, 2–40 %) based on Mie theory. All spectra are normalized at the highest peak. (B) ML-predicted model of the size deviation and FWHM. (C) Synthesis database using the ML model with multiple synthesis parameters and FWHM. (D) Calculated extinction spectra of Ag NCs with different average sizes (diameter, 30–220 nm) based on Mie theory. All spectra are normalized at 267 nm. (E) ML-predicted model of the average size and dipolar peak position. (F) Relationship between the diameter of Ag NCs and the particle number of additional seeds under different optimal conditions for homogeneous synthesis described in (C).

synthesis model (Fig. 2C), more experiments (Table S5) are performed to verify the applicability of the model. In comparison, the Ag NCs synthesized under different optimal conditions have almost the same optical properties (Fig. S14). These results demonstrate that the established model can be used to synthesize Ag layers with a uniform shape and size.

The actual sizes obtained by the ML-predicted model (Fig. 2E) are fitting well with the number of additional Ag-NC seeds (Fig. 2F and Fig. S15) according to the classical growth model shown by equation (1) [14,19,49]:

$$D = \left[\frac{6}{\pi}(m + \Delta m)/\rho N\right]^{\frac{1}{3}} \quad (1)$$

where D is the calculated diameter of Ag NCs, π is a constant, m is the Ag mass of additional seeds, Δm is the Ag mass of additional silver nitrate, ρ is the Ag density, N is the particle number of Ag NCs and equal to the particle number of additional seeds. The coefficient of determination (R^2 greater than 0.99, Fig. S15) between the actual and calculated diameters of Ag NCs is close to 1 in the training dataset, indicating that the actual size of Ag NCs can be precisely controlled by simply adjusting the number of additional Ag-NC seeds under the optimal conditions predicted by the model without secondary nucleation and Ag loss. The yields of Ag NCs synthesized under multi-parameter optimizations for homogeneous growth are above 99 %. These results demonstrate that the model of multiple parameters established for uniform synthesis can be further matched with the classical growth model to achieve the size control of Ag NCs.

3.2. Optical characterization of Ag NCs

Based on the perfect match between the synthesis model and the growth model discussed above, Ag NCs with different sizes but regular gaps are fabricated and analyzed optically using the automated platform (Fig. 3, Table S6). The extinction spectra of Ag NCs change with their average sizes in the visible and near-infrared regions (Fig. 3A), and the different colors are consistent with extinction spectra (inset in Fig. 3A) related to the different SPR effects of Ag NCs with different sizes.

The SPR peaks in extinction spectra of Ag NCs with different sizes, including the dipolar mode, quadrupole mode, and octupole mode, are compared in Fig. 3B. Generally, the location of the dipolar SPR peak extends to longer wavelengths with size (Fig. 3B). For instance, when the size of Ag NCs goes up from 24 to 230 nm, the dipolar mode gradually redshifts from 400 to 852 nm (Table S8). Additionally, the symmetrical dipolar peaks widen due to the radiative losses with increasing sizes and the nonzero baselines become obvious in the near-infrared region. Compared to the dipole SPR peak in extinction spectra of Ag NCs throughout the total size range, the quadrupole SPR peak appears in the size range between 82 and 230 nm. Similarly, the quadrupole SPR peak progressively redshifts from 400 to 551 nm as the size of Ag NCs increases from 82 to 230 nm. When the Ag NCs are bigger than 174 nm, the octopolar mode gradually evolves as the main SPR peak in extinction spectra and redshifts from 412 to 454 nm when the size of Ag NCs goes up from 174 to 230 nm. By matching the widest range of the dipole peak in comparison with the other higher SPR peaks, the actual size of Ag NCs can be determined. Fig. 3C shows the linear relationship between the calculated diameters based on the classical growth model (equation (1), Fig. S16) and the actual diameters determined from Ag NCs by the ML-predicted model (Fig. 2E), demonstrating that the size of Ag NCs can be controlled preciously and they have nearly ideal spherical optical properties.

Fig. 3D shows the RGB color photo of Ag NCs with different sizes captured by a camera (inset in Fig. 3A). In general, the color of Ag NCs changes gradually from yellow to orange, purple, blue, cyan, and grey as their size increases. The colors can be incorporated into the empirical

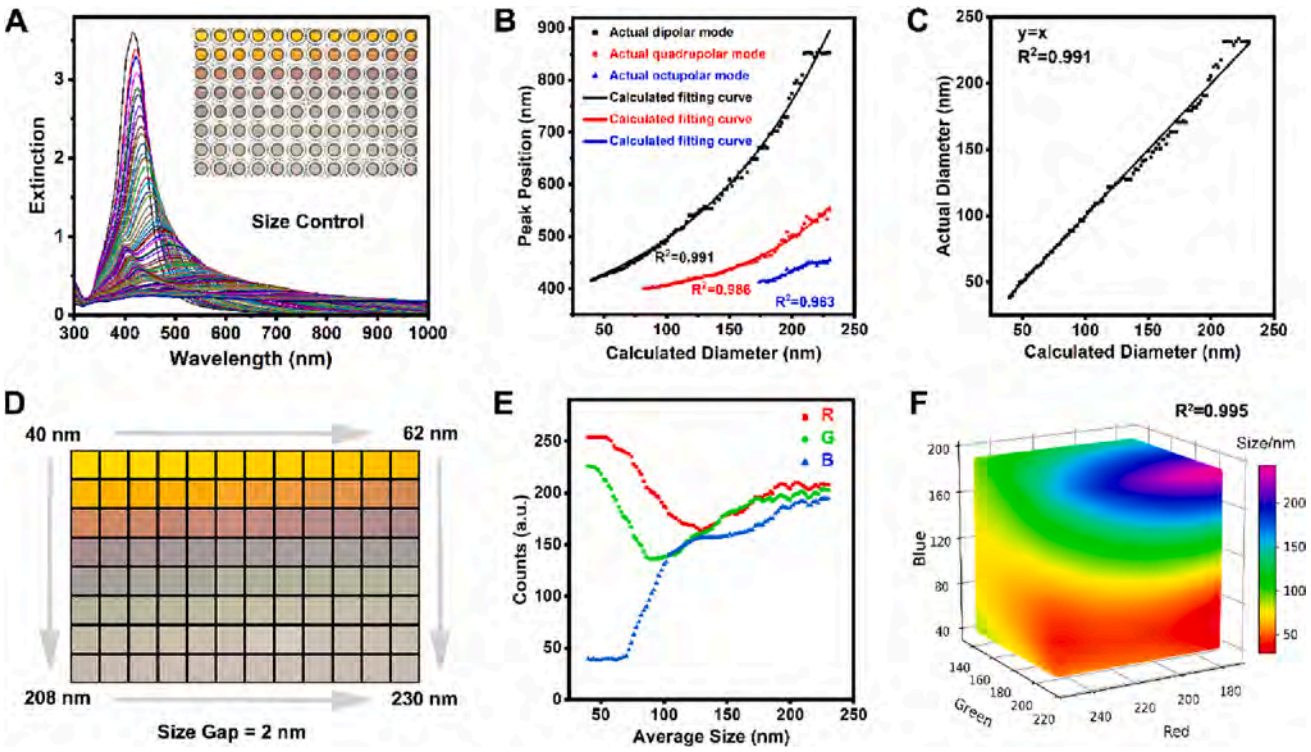

Fig. 3. Optical characterization of Ag NCs with size control. (A) Extinction spectra of Ag NCs with different calculated sizes (40–230 nm, 2 nm size gap) with the inset showing the high-quality digital photo of Ag NCs on the microplate. (B) ML models of the calculated size and peak position including the dipolar peak, quadrupolar peak, and octupolar peak. (C) Linear relationship between the calculated sizes by the classical growth model and actual sizes by the ML-predicted model. (D) RGB color-block photo of Ag NCs with different sizes recorded by a camera on the robotic platform. (E) Scatter plot of the RGB values and average sizes of Ag NCs. (F) Color database of the ML model with RGB values and average sizes of Ag NCs.

database for visual identification of the size of Ag NCs (Table S9). The RGB values of Ag NCs are presented in Fig. 3E for digital analysis, and the ML model for RGB values and average sizes is established as shown in Fig. 3F. The training dataset is in good agreement with the values predicted by the ML model (R^2 greater than 0.99, Table S10 and Fig. S17), demonstrating that the ML model is accurate and can be used to guide the digital analysis of the color of Ag NCs. It is noted that the RGB value refers to the color brightness [50] and so the practicability of the established model is limited due to the fixed amount of Ag in this case. Nonetheless, these results indicate that the colors of Ag NCs with different sizes can be monitored easily on the automated platform after controllable synthesis and digital analysis to establish the intrinsic relationship between average size and optical property.

3.3. Scaling up of Ag NCs

On the basis of data screening and high-throughput experiments, the databases of Ag NCs including controllable synthesis and optical properties are visually established with ML models, which are used to optimize and scale up the synthesis of Ag NCs. Specifically, the scale-up experiments (selecting Ag NCs with four average sizes, Fig. 4A) are presented by proportionally expanding the synthesis volume from 1 to 1,000 mL based on the same recipes from established models. One can clearly see that the colloid colors and spectral peak positions of Ag NCs obtained in different volumes are almost the same (Fig. 4B). The Ag NCs obtained in different volumes have the same size and distribution on the basis of optimized re-synthesis (Fig. S18 and Table S11), revealing a relatively simple and effective way for mass production of Ag NCs with high quality. In short, more than 1,200 valid samples in the experimental database have been synthesized to establish the ML models of Ag NCs. Taking the advantage of AI (Table S12), the robust database of multi-parameter controllable synthesis is better than those reported previously [13–15,19,20,37,45,49].

TEM images in Fig. 4C are acquired from Ag NCs with different sizes in the largest volumes (1,000 mL), and the actual sizes are 50 ± 5, 100 ± 8, 150 ± 12, and 200 ± 15 nm, respectively. The results disclose that all spherical Ag NCs have narrow normal distributions (SD less than 10 %) and expected average sizes, in agreement with the spectral results (FWHM and peak position). Additionally, low-magnification TEM images are also shown in Fig. S19, indicating the high yields of Ag NCs with uniform size distribution and ideal spherical morphology. The average sizes and optical properties of Ag NCs are consistent with the simulated results consequently validating the practicality and scalability of the ML models using this platform and optimized re-synthesis of Ag NCs beyond the platform. Moreover, the X-ray diffraction (XRD) patterns of the synthesized Ag NCs show five distinct peaks around 38°, 44°, 64°, 77° and 81° in the 2θ region (Fig. 4D), which are assigned to (111), (200), (220), (311) and (222) planes, respectively. The obtained Bragg's reflections are indexed on the basis of the fcc structure of standard Ag atoms (JCPDS card No. 04–0783). The FWHM of the XRD peak becomes narrow with the increase of particle size, demonstrating that the crystallinity of Ag NCs becomes better with the growth. And as shown in the high-resolution TEM (HRTEM) image and selected area electron diffraction (SAED) pattern of the single particle (Fig. 4E), the synthesized Ag NC exhibits polycrystalline structures with diffraction rings.

The lifetime analysis of Ag NC synthesized by mass production is displayed in Fig. 4F. It can be clearly seen that the intensity and FWHM of extinction peak of Ag NCs have almost no change within 50 days after fresh synthesis, indicating that there is no significant change in the morphology and size distribution of Ag NCs in storage. And the quality of Ag NCs obviously deteriorates after 90 days of storage. Moreover, extinction spectra of freshly synthesized Ag NCs with different sizes overlap well with those after 6 weeks of storage (Fig. S20), indicating that the synthesized Ag NCs have strong stability against aggregation

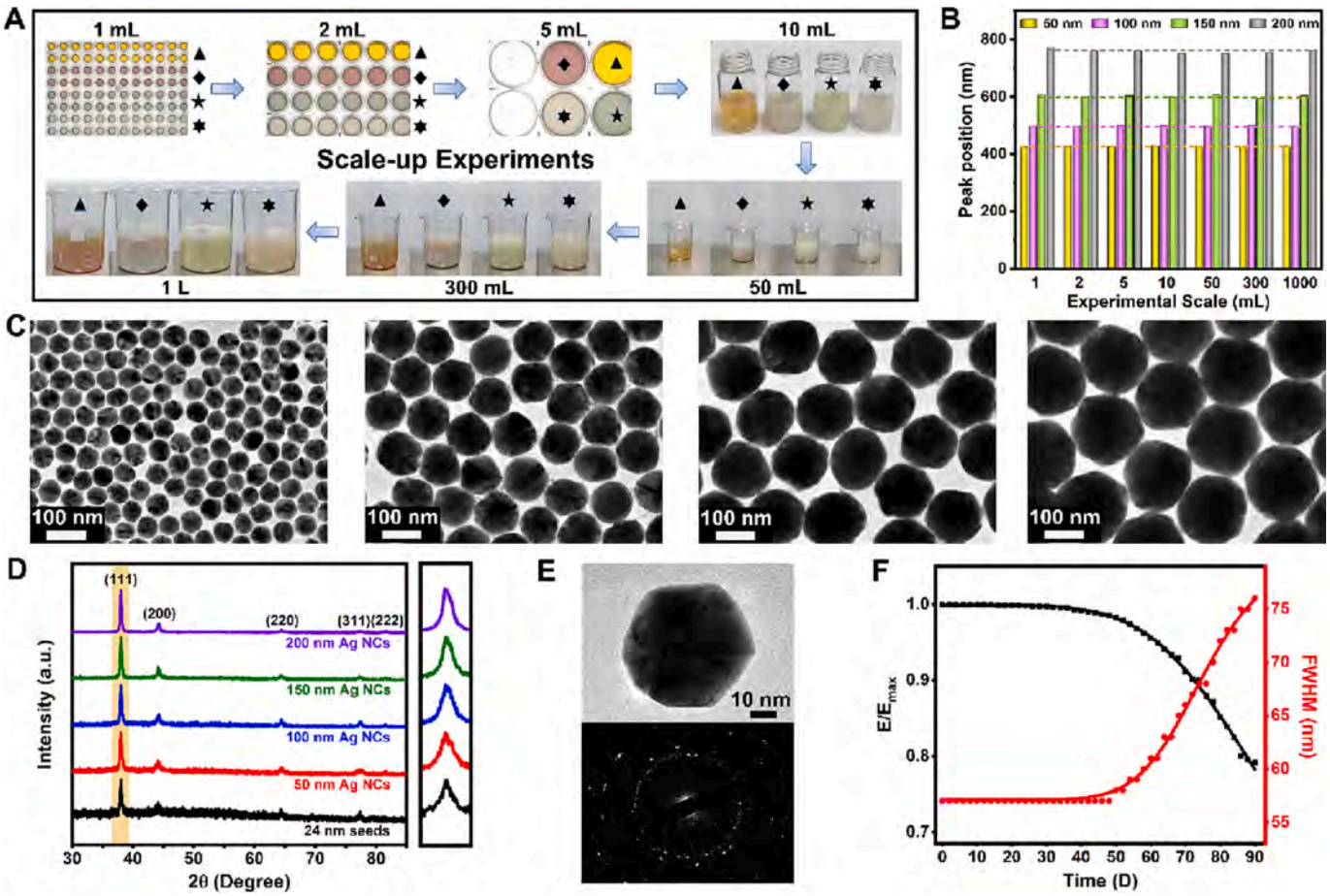

Fig. 4. Scale-up explorations of Ag NCs beyond the platform. (A) Scale-up experiments of Ag NCs with four average sizes (50, 100, 150, and 200 nm) by increasing the volume from 1 to 1,000 mL. (B) Histogram of the dipolar peak positions of Ag NCs synthesized in different volumes. (C) TEM images of the synthesized Ag NCs with different sizes (50, 100, 150, and 200 nm from left to right). (D) XRD patterns of the synthesized Ag NCs with different sizes, the inset on the right is a partial enlargement of the yellow area. (E) HRTEM image and SAED pattern of 50 nm single-particle Ag NC. (F) Lifetime analysis of 50 nm synthesized Ag NCs by recording the intensity change (black line) and FWHM (red line) of their extinction spectra. (For interpretation of the references to color in this figure legend, the reader is referred to the web version of this article.)

and chemical dissolution for subsequent use. These results demonstrate that Ag NCs synthesized without polymers can maintain a good shape, size, and narrow distribution for a long time with TSC as stabilizing agents.

3.4. Application of Ag NCs for Hg^{2+} detection

As discussed above, the optical properties of Ag NCs greatly depend on their shape and size, which affect the reproducibility and sensitivity in optical applications. Homogeneous Ag NCs are often used for the optical detection of hazardous substances due to their high SPR efficiency and the dipolar efficiency reaches the maximum at about 50 nm (Fig. 5A), indicating a large signal response in colorimetric detection. Thus, the colloidal dispersions containing 50 nm Ag NCs are selected for Hg^{2+} detection by colorimetry.

As shown in Fig. S21, typical interferences are investigated *in situ* on the platform. Compared with other metal ions including Na^{+}, K^{+}, Li^{+}, Mg^{2+}, Ca^{2+}, Zn^{2+}, Al^{3+}, Fe^{2+}, Fe^{3+}, Co^{2+}, Ni^{2+}, Ti^{4+}, Cu^{2+}, Cd^{2+}, Cr^{3+}, Mn^{2+}, Sr^{2+}, Zr^{4+}, Ag^{+}, Ba^{2+}, Pb^{2+}, and Ga^{3+}, the changing ratio ($\Delta E/E_{max}$) of the extinction value of the dipolar peak of Ag NCs after addition of Hg^{2+} was much larger for the same high concentration (Fig. 5B). Accordingly, the color of the dispersion containing Hg^{2+} changes from yellow to dark grey, whereas the color of the dispersions remains almost the same after addition of the other metal ions (Fig. 5C). The high selectivity can be further explained by the fact that the redox potential of Hg^{2+}/Hg (0.845 V) is higher than that of Ag^{+}/Ag (0.799 V), while other interfering cations have lower redox potentials [16,51]. The significantly reduced intensity of extinction peaks confirms the occurrence of the redox reaction, as shown in equation (2). The change of XRD patterns of Ag NCs after the addition of Hg^{2+} (Fig. S22) further indicates that the crystal structures of Ag NCs as optical sensors are obviously etched by Hg^{2+}.

$$2Ag(s) + Hg^{2+}(aq) \rightarrow 2Ag^{+}(aq) + Hg(s) \quad (2)$$

One of the advantages of the database established is to produce stable colloidal dispersions of Ag NCs with weak ligands (TSC-Ag NCs), which can be displaced easily by other long-chain polymers. As shown in Fig. 5D, the possibility of modification of TSC-Ag NCs has been demonstrated by ligand exchange with PVP and GEL, which have high chemical affinities to Ag. The characteristic peaks of Fourier transform infrared (FT-IR) spectra of PVP-Ag NCs and GEL-Ag NCs change significantly after the ligand exchange of TSC-Ag NCs, indicating that the long-chain polymers have replaced original TSC ligands as functional groups on the surface of Ag NCs (Fig. S23). As the molecular weight of the surface ligand increases, the variation in extinction intensity of Ag NCs to Hg^{2+} concentration decreases (Fig. S24 and S25). The color changes of TSC-Ag NCs are more sensitive than those modified with polymers, while the color changes of PVP-Ag NCs and GEL-Ag NCs are more abundant at higher Hg^{2+} concentrations (Fig. 5E). This obvious difference in the photochemical change of Ag NCs can be explained by

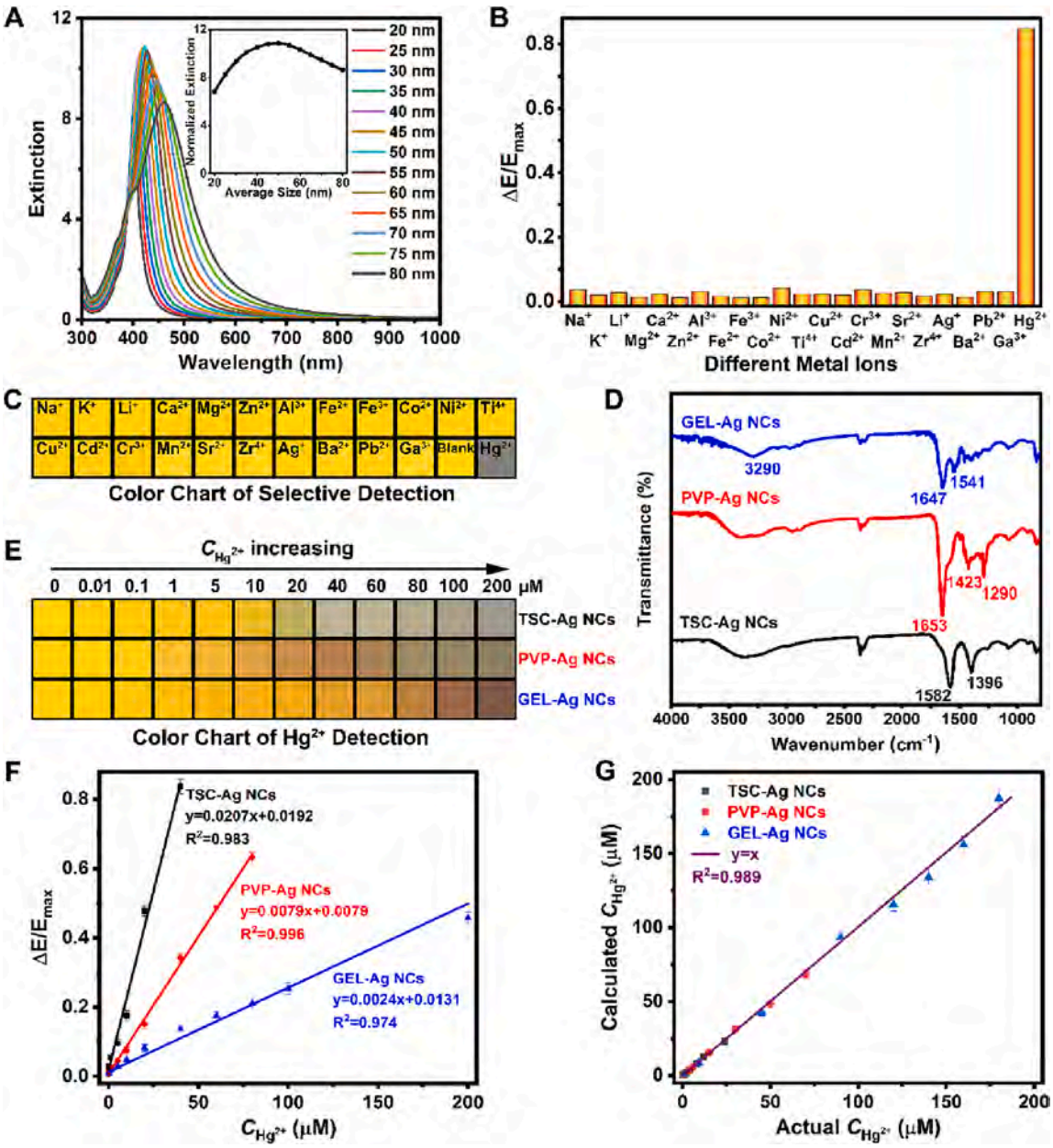

Fig. 5. Application of Ag NCs for Hg^{2+} detection by colorimetry. (A) Calculated extinction spectra of Ag NCs with different sizes at fixed particle numbers, the inset exhibits the normalized efficiency of dipolar peaks. (B) Histogram of the changing ratio ($\Delta E/E_{max}$) of extinction intensities of Ag NCs after the addition of different metal ions (0.2 mM). (C) RGB color-block photo of Ag NCs for Hg^{2+} selective detection in various metal ions. (D) FT-IR spectra of Ag NCs modified with different surface ligands including TSC, PVP, and GEL. (E) RGB color-block photo of Ag NCs modified with different surface ligands for Hg^{2+} detection. (F) Linear curves of the changing ratios of extinction intensities of Ag NCs with Hg^{2+} concentrations. (G) Scatter plot of the actual Hg^{2+} and calculated Hg^{2+} concentrations.

the density of the surface coatings which hinder the diffusion and reaction of Hg^{2+}. The results demonstrate that the surface chemistry of Ag NCs is critical to visual detection and further modifications broaden the detection ranges of Hg^{2+} at higher concentrations.

Since Ag NCs modified with various ligands exhibit uniformity and reproducibility in color change, quantitative determination of Hg^{2+} concentration (C) is carried out by colorimetry. Since the signal-to-noise ratio (S/N) is greater than 3, the changing ratios of extinction intensities of TSC-Ag NCs, PVP-Ag NCs, and GEL-Ag NCs bear linear relationships with Hg^{2+} concentrations from 0.01 to 40 μM, 0.01 to 80 μM, and 0.1 to 200 μM, respectively (Fig. S26). The standard curves (R^2 greater than 0.97) for quantitative detection of Hg^{2+} are established (Fig. 5F), and the concentration of Hg^{2+} can be determined quantitatively in the linear range of 0.01 to 200 μM with a detection limit (S/N = 3) of 3 nM. The modification of surface ligands of Ag NCs can coordinate their performance in Hg^{2+} detection as colorimetric sensors. Compared with other Hg^{2+} colorimetric sensors reported recently [5,16,51–56], the sensitivity of prepared Ag NCs is much better, especially in terms of the ultrabroad linear range (Table S13).

In order to investigate the commercial feasibility, a series of real samples are further tested (Table S14). The sample recoveries are between 94.8 and 105.6 %, and the relative standard deviations (RSDs) are between 1.67 and 3.33 %. The excellent linear relationship ($R^2 = 0.989$) between the actual and calculated concentration verifies the reliability and practicality of Hg^{2+} quantitative detection on the robotic platform (Fig. 5G). The synthesized Ag NCs with various ligands can still maintain a good linear response with expected results in samples of river water. These results demonstrate that the platform can achieve the efficient and

high-throughput screening of stable Ag NCs for colorimetric quantitative analysis in real water. Moreover, interference study in real samples is also investigated *in situ* on the platform (Fig. S27). It is found that the synthesized Ag NCs as optical sensors have good stability and strong selectivity for Hg^{2+} detection in real water. Generally, the benefits of the new approach against existing state-of-the-art practices (Table S15) have been proved with the help of technological development [27,28,30–33,36,37,41].

4. Conclusions

In this study, an automated high-throughput platform is established for the wet-chemical synthesis and optical characterization of colloidal Ag NCs. The ML-predicted models of FWHM and peak positions are constructed by optical simulation and adopted as data-driven models to evaluate the uniformity and nanoscale of Ag NCs. According to the experimental database of more than 1,200 valid samples, the ML model incorporating multiple synthesis parameters is established for uniform synthesis and can further match the classical growth model to achieve size control of Ag NCs. On the basis of the controllable synthesis, the database is established for the optical properties of Ag NCs and digitized to correlate with their size. Optimized manual re-synthesis of high-quality Ag NCs validates the practical feasibility and scalability of established models. The TSC-Ag NCs can be modified by polymer ligands (PVP, GEL) as colorimetric sensors for efficient and quantitative detection of Hg^{2+} in the linear concentration range of 0.01 to 200 μM with a detection limit of 3 nM. The results demonstrate the controllable synthesis of Ag NCs can be achieved to improve their reproducibility and sensitivity in Hg^{2+} determination on the robotic platform. Therefore, this work provides a new scientific strategy for the high-throughput study of colloidal Ag NCs, including data-driven modeling of simulated information, automated synthesis and characterization in wet chemistry, ML optimization of multiple parameters, and *in situ* screening in color application. AI in chemistry is expected to attract more attention and particular interest to accelerate the development of advanced optical materials.

5. Data availability

No data was used for the research described in the article.

Declaration of Competing Interest

The authors declare that they have no known competing financial interests or personal relationships that could have appeared to influence the work reported in this paper.

Data availability

No data was used for the research described in the article.

Acknowledgements

This work is financially supported by National Natural Science Foundation of China (52173234, 21975280), Shenzhen-Hong Kong-Macau Technology Research Program (Type C, SGDX2020110309300301), Shenzhen Science and Technology Program (Grant No. RCJC20200714114435061, JCYJ20210324102008023 and JSGG20210802153408024), Natural Science Foundation of Guangdong Province (2022A1515010554), CCF-Tencent Open Fund, City University of Hong Kong Strategic Research Grant (SRG No. 7005505), and City University of Hong Kong Donation Research Grant (DON-RMG No. 9229021).

Appendix A. Supplementary data

Supplementary data to this article can be found online at https://doi.org/10.1016/j.cej.2023.143225.

References

[1] K.-H. Kim, E. Kabir, S.A. Jahan, A review on the distribution of Hg in the environment and its human health impacts, J. Hazard. Mater. 306 (2016) 376–385, https://doi.org/10.1016/j.jhazmat.2015.11.031.
[2] H. Zhao, G. Yang, X. Gao, C.H. Pang, S.W. Kingman, T. Wu, Hg^0 capture over CoMoS/γ-Al_2O_3 with MoS_2 nanosheets at low temperatures, Environ. Sci. Technol. 50 (2016) 1056–1064, https://doi.org/10.1021/acs.est.5b04278.
[3] M. Xu, X. Wang, X. Liu, Detection of heavy metal ions by ratiometric photoelectric sensor, J. Agric. Food Chem. 70 (2022) 11468–11480, https://doi.org/10.1021/acs.jafc.2c03916.
[4] L. Huang, Q. Zhu, J. Zhu, L. Luo, S. Pu, W. Zhang, W. Zhu, J. Sun, J. Wang, Portable colorimetric detection of mercury(II) based on a non-noble metal nanozyme with tunable activity, Inorg. Chem. 58 (2019) 1638–1646, https://doi.org/10.1021/acs.inorgchem.8b03193.
[5] A. Amirjani, D.F. Haghshenas, Facile and on−line colorimetric detection of Hg^{2+} based on localized surface plasmon resonance (LSPR) of Ag nanotriangles, Talanta 192 (2019) 418–423, https://doi.org/10.1016/j.talanta.2018.09.079.
[6] X. Zhang, C. Sun, L. Zhang, H. Liu, B. Cao, L. Liu, W. Gong, Adsorption studies of cadmium onto magnetic Fe_3O_4@$FePO_4$ and its preconcentration with detection by electrothermal atomic absorption spectrometry, Talanta 181 (2018) 352–358, https://doi.org/10.1016/j.talanta.2018.01.023.
[7] X. Wang, C. Shen, C. Zhou, Y. Bu, X. Yan, Methods, principles and applications of optical detection of metal ios, Chem. Eng. J. 417 (2021), 129125, https://doi.org/10.1016/j.cej.2021.129125.
[8] D. Zhang, S. Yang, Q. Ma, J. Sun, H. Cheng, Y. Wang, J. Liu, Simultaneous multi-elemental speciation of As, Hg and Pb by inductively coupled plasma mass spectrometry interfaced with high-performance liquid chromatography, Food Chem. 313 (2020), 126119, https://doi.org/10.1016/j.foodchem.2019.126119.
[9] L. Tang, J. Li, Plasmon-based colorimetric nanosensors for ultrasensitive molecular diagnostics, ACS Sens. 2 (2017) 857–875, https://doi.org/10.1021/acssensors.7b00282.
[10] J. Tao, S. Chen, E.K. Fodjo, W. Deng, D. Li, Tailoring dual-functional gold nanoplasmonic rods for colorimetric and SERS detection of mercury species in complex matrices, Chem. Eng. J. 452 (2023), 139026, https://doi.org/10.1016/j.cej.2022.139026.
[11] C. Gao, Z. Lu, Y. Liu, Q. Zhang, M. Chi, Q. Cheng, Y. Yin, Highly stable silver nanoplates for surface plasmon resonance biosensing, Angew. Chem. Int. Ed. 51 (2012) 5629–5633, https://doi.org/10.1002/anie.201108971.
[12] R.K. Sharma, S. Yadav, S. Dutta, H.B. Kale, I.R. Warkad, R. Zboril, R.S. Varma, M. B. Gawande, Silver nanomaterials: synthesis and (electro/photo) catalytic applications, Chem. Soc. Rev. 50 (2021) 11293–11380, https://doi.org/10.1039/d0cs00912a.
[13] N.G. Bastus, F. Merkoci, J. Piella, V. Puntes, Synthesis of highly monodisperse citrate-stabilized silver nanoparticles of up to 200 nm: kinetic control and catalytic properties, Chem. Mater. 26 (2014) 2836–2846, https://doi.org/10.1021/cm500316k.
[14] L. Xing, Y. Xiahou, P. Zhang, W. Du, H. Xia, Size control synthesis of monodisperse, quasi-spherical silver nanoparticles to realize surface-enhanced Raman scattering uniformity and reproducibility, ACS Appl. Mater. Interfaces 11 (2019) 17637–17646, https://doi.org/10.1021/acsami.9b02052.
[15] L. Zhang, Z. Huang, Y. Han, Z. Guo, X. Zhang, R. Xie, W. Yang, Histidine-directed formation of nearly monodispersed silver nanoflowers and their ultra-high peroxidase-like activity under physiological pH, Appl. Surf. Sci. 532 (2020), 147457, https://doi.org/10.1016/j.apsusc.2020.147457.
[16] Monisha, K. Shrivas, T. Kant, S. Patel, R. Devi, N.S. Dahariya, S. Pervez, M.K. Deb, M.K. Rai, J. Rai, Rai, Inkjet-printed paper-based colorimetric sensor coupled with smartphone for determination of mercury (Hg^{2+}), J. Hazard. Mater. 414 (2021) 125440.
[17] K. Nathanael, P. Pico, N.M. Kovalchuk, A.D. Lavino, M.J.H. Simmons, O.K. Matar, Computational modelling and microfluidics as emerging approaches to synthesis of silver nanoparticles – A review, Chem. Eng. J. 436 (2022), 135178, https://doi.org/10.1016/j.cej.2022.135178.
[18] J. Zeng, Y. Zheng, M. Rycenga, J. Tao, Z.-Y. Li, Q. Zhang, Y. Zhu, Y. Xia, Controlling the shapes of silver nanocrystals with different capping agents, J. Am. Chem. Soc. 132 (2010) 8552–8553, https://doi.org/10.1021/ja103655f.
[19] X. Liu, Y. Yin, C. Gao, Size-tailored synthesis of silver quasi-nanospheres by kinetically controlled seeded growth, Langmuir 29 (2013) 10559–10565, https://doi.org/10.1021/la402147f.
[20] Z. Chen, J.W. Chang, C. Balasanthiran, S.T. Milner, R.M. Rioux, Anisotropic growth of silver nanoparticles is kinetically controlled by polyvinylpyrrolidone binding, J. Am. Chem. Soc. 141 (2019) 4328–4337, https://doi.org/10.1021/jacs.8b11295.
[21] L. Xing, Y. Xiahou, X. Zhang, W. Du, P. Zhang, H. Xia, Large-area monolayer films of hexagonal close-packed Au@Ag nanoparticles as substrates for SERS-based quantitative determination, ACS Appl. Mater. Interfaces 14 (2022) 13480–13489, https://doi.org/10.1021/acsami.1c23638.
[22] M. Liu, K. Liu, C. Gao, Effects of ligands on synthesis and surface-engineering of noble metal nanocrystals for electrocatalysis, ChemElectroChem. 9 (2022) e202200651.

[23] B.I. Karawdeniya, A.M. Damry, K. Murugappan, S. Manjunath, Y.M.N.D. Y. Bandara, C.J. Jackson, A. Tricoli, D. Neshev, Surface functionalization and texturing of optical metasurfaces for sensing applications, Chem. Rev. 122 (2022) 14990–15030, https://doi.org/10.1021/acs.chemrev.1c00990.
[24] J.-J. Zhu, W. Dressel, K. Pacion, Z.J. Ren, *ES&T* in the 21st century: a data-driven analysis of research topics, interconnections, and trends in the past 20 years, Environ. Sci. Technol. 55 (2021) 3453–3464, https://doi.org/10.1021/acs.est.0c07551.
[25] Q. Zhu, F. Zhang, Y. Huang, H. Xiao, L. Zhao, X. Zhang, T. Song, X. Tang, X. Li, G. He, B. Chong, J. Zhou, Y. Zhang, B. Zhang, J. Cao, M. Luo, S. Wang, G. Ye, W. Zhang, X. Chen, S. Cong, D. Zhou, H. Li, J. Li, G. Zou, W. Shang, J. Jiang, Y. Luo, An all-round AI-chemist with a scientific mind, Nat. Sci. Rev. 9 (2022) nwac190. https://doi.org/10.1093/nsr/nwac190.
[26] D.P. Tabor, L.M. Roch, S.K. Saikin, C. Kreisbeck, D. Sheberla, J.H. Montoya, S. Dwaraknath, M. Aykol, C. Ortiz, H. Tribukait, C. Amador-Bedolla, C.J. Brabec, B. Maruyama, K.A. Persson, A. Aspuru-Guzik, Accelerating the discovery of materials for clean energy in the era of smart automation, Nat. Rev. Mater. 3 (2018) 5–20, https://doi.org/10.1038/s41578-018-0005-z.
[27] S. Steiner, J. Wolf, S. Glatzel, A. Andreou, J.M. Granda, G. Keenan, T. Hinkley, G. Aragon-Camarasa, P.J. Kitson, D. Angelone, L. Cronin, Organic synthesis in a modular robotic system driven by a chemical programming language, Science 363 (6423) (2019), https://doi.org/10.1126/science.aav2211.
[28] Y. Zhao, T. Heumueller, J. Zhang, J. Luo, O. Kasian, S. Langner, C. Kupfer, B. Liu, Y. Zhong, J. Elia, A. Osvet, J. Wu, C. Liu, Z. Wan, C. Jia, N. Li, J. Hauch, C. J. Brabec, A bilayer conducting polymer structure for planar perovskite solar cells with over 1,400 hours operational stability at elevated temperatures, Nat. Energy 7 (2021) 144–152, https://doi.org/10.1038/s41560-021-00953-z.
[29] L. Buglioni, F. Raymenants, A. Slattery, S.D.A. Zondag, T. Noël, Technological innovations in photochemistry for organic synthesis: flow chemistry, high-throughput experimentation, scale-up, and photoelectrochemistry, Chem. Rev. 122 (2022) 2752–2906, https://doi.org/10.1021/acs.chemrev.1c00332.
[30] J.M. Granda, L. Donina, V. Dragone, D.-L. Long, L. Cronin, Controlling an organic synthesis robot with machine learning to search for new reactivity, Nature 559 (2018) 377–381, https://doi.org/10.1038/s41586-018-0307-8.
[31] R.L. Greenaway, V. Santolini, M.J. Bennison, B.M. Alston, C.J. Pugh, M.A. Little, M. Miklitz, E.G.B. Eden-Rump, R. Clowes, A. Shakil, H.J. Cuthbertson, H. Armstrong, M.E. Briggs, K.E. Jelfs, A.I. Cooper, High-throughput discovery of organic cages and catenanes using computational screening fused with robotic synthesis, Nat. Commun. 9 (2018) 2849, https://doi.org/10.1038/s41467-018-05271-9.
[32] N. Hartrampf, A. Saebi, M. Poskus, Z.P. Gates, A.J. Callahan, A.E. Cowfer, S. Hanna, S. Antilla, C.K. Schissel, A.J. Quartararo, X. Ye, A.J. Mijalis, M.D. Simon, A. Loas, S. Liu, C. Jessen, T.E. Nielsen, B.L. Pentelute, Synthesis of proteins by automated flow chemistry, Science 368 (2020) 980–987, https://doi.org/10.1126/science.abb2491.
[33] G.-N. Ahn, J.-H. Kang, H.-J. Lee, B.E. Park, M. Kwon, G.-S. Na, H. Kim, D.-H. Seo, D.-P. Kim, Exploring ultrafast flow chemistry by autonomous self-optimizing platform, Chem. Eng. J. 453 (2023), 139707, https://doi.org/10.1016/j.cej.2022.139707.
[34] H. Tao, T. Wu, M. Aldeghi, T.C. Wu, A. Aspuru-Guzik, E. Kumacheva, Nanoparticle synthesis assisted by machine learning, Nat. Rev. Mater. 6 (2021) 701–716, https://doi.org/10.1038/s41578-021-00337-5.
[35] F. Lai, Z. Sun, S.E. Saji, Y. He, X. Yu, H. Zhao, H. Guo, Z. Yin, Machine learning-aided crystal facet rational design with ionic liquid controllable synthesis, Small 17 (2021) 2100024, https://doi.org/10.1002/smll.202100024.
[36] K. Higgins, M. Ziatdinov, S.V. Kalinin, M. Ahmadi, High-throughput study of antisolvents on the stability of multicomponent metal halide perovskites through robotics-based synthesis and machine learning approaches, J. Am. Chem. Soc. 143 (2021) 19945–19955, https://doi.org/10.1021/jacs.1c10045.
[37] H. Tao, T. Wu, S. Kheiri, M. Aldeghi, A. Aspuru-Guzik, E. Kumacheva, Self-driving platform for metal nanoparticle synthesis: combining microfluidics and machine learning, Adv. Funct. Mater. 31 (2021) 2106725, https://doi.org/10.1002/adfm.202106725.
[38] N.A. Jose, M. Kovalev, E. Bradford, A.M. Schweidtmann, H. Chun Zeng, A. A. Lapkin, Pushing nanomaterials up to the kilogram scale – an accelerated approach for synthesizing antimicrobial ZnO with high shear reactors, machine learning and high-throughput analysis, Chem. Eng. J. 426 (2021), 131345, https://doi.org/10.1016/j.cej.2021.131345.
[39] X. Liu, X. Wang, S. Gao, V. Chang, R. Tom, M. Yu, L.M. Ghiringhelli, N. Marom, Finding predictive models for singlet fission by machine learning, npj Comput, Mater. 8 (2022) 70, https://doi.org/10.1038/s41524-022-00758-y.
[40] E.S. Isbrandt, R.J. Sullivan, S.G. Newman, High throughput strategies for the discovery and optimization of catalytic reactions, Angew. Chem. Int. Ed. 58 (2019) 7180–7191, https://doi.org/10.1002/anie.201812534.
[41] P. Chen, Z. Tang, Z. Zeng, X. Hu, L. Xiao, Y. Liu, X. Qian, C. Deng, R. Huang, J. Zhang, Y. Bi, R. Lin, Y. Zhou, H. Liao, D. Zhou, C. Wang, W. Lin, Machine-learning-guided morphology engineering of nanoscale metal-organic frameworks, Matter 2 (2020) 1651–1666, https://doi.org/10.1016/j.matt.2020.04.021.
[42] Y. Yao, Q. Dong, A. Brozena, J. Luo, J. Miao, M. Chi, C. Wang, I.G. Kevrekidis, Z. J. Ren, J. Greeley, G. Wang, A. Anapolsky, L. Hu, High-entropy nanoparticles: synthesis-structure-property relationships and data-driven discovery, Science. 376 (2022) eabn3103, https://doi.org/10.1126/science.abn3103.
[43] Q. Fu, W. Sun, Mie theory for light scattering by a spherical particle in an absorbing medium, Appl. Opt. 40 (2001) 1354–1361, https://doi.org/10.1364/AO.40.001354.
[44] I. Niskanen, V. Forsberg, D. Zakrisson, S. Reza, M. Hummelgård, B. Andres, I. Fedorov, T. Suopajärvi, H. Liimatainen, G. Thungström, Determination of nanoparticle size using rayleigh approximation and Mie theory, Chem. Eng. Sci. 201 (2019) 222–229, https://doi.org/10.1016/j.ces.2019.02.020.
[45] H. Li, H. Xia, D. Wang, X. Tao, Simple synthesis of monodisperse, quasi-spherical, citrate-stabilized silver nanocrystals in water, Langmuir 29 (2013) 5074–5079, https://doi.org/10.1021/la400214x.
[46] Y. Jia, X. Hou, Z. Wang, X. Hu, Machine learning boosts the design and discovery of nanomaterials, ACS Sustain. Chem. Eng. 9 (2021) 6130–6147, https://doi.org/10.1021/acssuschemeng.1c00483.
[47] Y. He, Z. Sun, C. Hu, Z. Wang, H. Li, Z. Yin, D. Tang, Data-driven engineering descriptor and refined scale relations for predicting bubble departure diameter, Int. J. Heat Mass Transf. 195 (2022), 123078, https://doi.org/10.1016/j.ijheatmasstransfer.2022.123078.
[48] Z. Wang, Z. Sun, H. Yin, X. Liu, J. Wang, H. Zhao, C.H. Pang, T. Wu, S. Li, Z. Yin, X. Yu, Data-driven materials innovation and applications, Adv. Mater. 34 (2022) 2104113, https://doi.org/10.1002/adma.202104113.
[49] W. Leng, P. Pati, P.J. Vikesland, Room temperature seed mediated growth of gold nanoparticles: mechanistic investigations and life cycle assesment, Environ, Sci. Nano 2 (2015) 440–453, https://doi.org/10.1039/c5en00026b.
[50] G. de Carvalho Oliveira, C.C.S. Machado, D.K. Inácio, J.F. da Silveira Petruci, S. G. Silva, RGB color sensor for colorimetric determinations: evaluation and quantitative analysis of colored liquid samples, Talanta 241 (2022), 123244, https://doi.org/10.1016/j.talanta.2022.123244.
[51] J.-K. Chen, S.-M. Zhao, J. Zhu, J.-J. Li, J.-W. Zhao, Colorimetric determination and recycling of Hg^{2+} based on etching-induced morphology transformation from hollow AuAg nanocages to nanoboxes, J. Alloys Compd. 828 (2020), 154392, https://doi.org/10.1016/j.jallcom.2020.154392.
[52] D. Huang, X. Liu, C. Lai, L. Qin, C. Zhang, H. Yi, G. Zeng, B. Li, R. Deng, S. Liu, Y. Zhang, Colorimetric determination of mercury(II) using gold nanoparticles and double ligand exchange, Microchim Acta 186 (2019) 31, https://doi.org/10.1007/s00604-018-3126-6.
[53] R. Liu, L. Zuo, X. Huang, S. Liu, G. Yang, S. Li, C. Lv, Colorimetric determination of lead(II) or mercury(II) based on target induced switching of the enzyme-like activity of metallothionein-stabilized copper nanoclusters, Microchim Acta 186 (2019) 250, https://doi.org/10.1007/s00604-019-3360-6.
[54] Z. Lu, Y. Dang, C. Dai, Y. Zhang, P. Zou, H. Du, Y. Zhang, M. Sun, H. Rao, Y. Wang, Hollow MnFeO oxide derived from MOF@MOF with multiple enzyme-like activities for multifunction colorimetric assay of biomolecules and Hg^{2+}, J. Hazard. Mater. 403 (2021), 123979 https://doi.org/10.1016/j.jhazmat.2020.123979.
[55] X.J. Du, Y. Chen, L.Y. Qin, H.Q. Luo, N.B. Li, B.L. Li, Plasmonic gold nanoparticles stain hydrogels for the portable and high-throughput monitoring of mercury ions, Environ. Sci. Technol. 56 (2022) 1041–1052, https://doi.org/10.1021/acs.est.1c07217.
[56] L. Feng, L. Zhang, Y. Gong, Z. Du, X. Chen, X. Qi, X. Zhang, G. Mao, H. Wang, Hollow C@MoS_2 nanotubes with Hg^{2+}-triggered oxidase-like catalysis: a colorimetric method for detection of Hg^{2+} ions in wastewater, Sens. Actuators B 361 (2022), 131725, https://doi.org/10.1016/j.snb.2022.131725.

Supplementary Material

Robotic Platform for Accelerating the High-throughput Study of Silver Nanocrystals in Sensitive/Selective Hg^{2+} Detection

Lixiang Xing [a,b], *Zijian Chen* [b], *Wei Chen* [b], *Paul K. Chu* [c], *Xue-Feng Yu* [*,a,b,d], *Haitao Zhao* [*,a,b]

[a] Shenzhen Key Laboratory of Micro/Nano Biosensing, Shenzhen Institute of Advanced Technology, Chinese Academy of Sciences, Shenzhen, Guangdong 518055, P. R. China

[b] Materials Interfaces Center, Shenzhen Institute of Advanced Technology, Chinese Academy of Sciences, Shenzhen 518055, Guangdong, P. R. China

[c] Department of Physics, Department of Materials Science and Engineering, and Department of Biomedical Engineering, City University of Hong Kong, Tat Chee Avenue, Kowloon, Hong Kong, China

[d] Hubei Three Gorges Laboratory, Yichang, Hubei 443007, P. R. China

[*] Corresponding authors. E-mail: ht.zhao@siat.ac.cn (H. Zhao); xf.yu@siat.ac.cn (X.-F. Yu)

Experimental Section

Materials. Silver nitrate ($AgNO_3$), trisodium citrate dihydrate (TSC), ascorbic acid (AA), ammonia water ($NH_3 \cdot H_2O$, 25%), NaCl, KCl, $NiCl_2$, $MnCl_2$, $Pb(NO_3)_2$ and $Hg(NO_3)_2$ were purchased from Sinopharm Chemical Reagent Co. Ltd. LiCl, $MgCl_2$, $CaCl_2$, $ZnCl_2$, $AlCl_3$, $FeCl_2$, $FeCl_3$, $CoCl_2$, $Ti(NO_3)_4$, $CuCl_2$, $CdCl_2$, $CrCl_3$, $SrCl_2$, $ZrCl_4$, $BaCl_2$ and $Ga(NO_3)_3$ were ordered from Aladdin, China. Polyvinyl pyrrolidone (PVP, K15) and gelatin (GEL) were bought from Sigma-Aldrich. All chemical reagents were used as received without further treatment. The deionized water (18 MΩ cm) was used in experiments without special emphasis.

Preparation of Ag-NC seeds. Ag-NC seeds with small size were prepared according to the reported protocol.[1] Typically, the aqueous TSC solution (1.5 mL, 50 mM), the aqueous $AgNO_3$ solution (1 mL, 30 mM), and the aqueous NaCl solution (0.4 mL, 20 mM) were successively added to 2.1 mL of water under stirring at room temperature. After 5 min of premixing, the aqueous AA solution (1 mL, 15 mM) and the premixture were quickly added into 94 mL of the boiling water in succession. After continuously heating and stirring for 1 h, the resulting dispersion of Ag NCs was naturally cooled to room temperature. The average size of the Ag-NC seeds was about 24 nm according to the statistical result of TEM (Fig. S22) and the particle concentration of seeds in the original solution was calculated to be about 4.26×10^{11} mL^{-1} according to the equation (1):

$$n = \frac{6m}{\pi d^3 \rho N_A V} \qquad (1)$$

where n is the particle concentration of the as-prepared seeds in the original solution, m is the Ag mass and is derived from the amount of $AgNO_3$ used for the synthesis of seeds, π is a constant, d is the diameter of seeds, ρ is the Ag density, N_A is the Avogadro′s constant, V is the total volume of the resulting dispersion of seeds. Since some reagents (such as TSC, AA, etc.) are also used for the subsequent growth, excess reagents in the original solution of seeds must be removed to ensure the accuracy of the established models of subsequent experiments. The original solution of Ag-NC seeds was centrifuged (12000 rcf, 10 min) to remove the supernatant and then redispersed into deionized water, and the particle concentration of seeds

after redispersion remained the same as before with the calibration of extinction spectra of the aqueous solutions.

Colloidal stability of Ag NCs. The extinction spectra of the as-prepared Ag NCs in mass productions were recorded to evaluate their colloidal stability. Firstly, the colloidal solutions of Ag NCs obtained in mass productions were heating at 50 ℃ for 5 min to remove the excess ammonia water, which may destroy the shape-size and dispersion of Ag NCs in the long-term storage. After that, the colloidal solutions were naturally cooled to room temperature and stored with seal in dark places. The extinction spectra of the colloidal solutions were recorded during long-term storage for comparison. Noted that the colloidal solutions of Ag NCs with large sizes needed to be well mixed to prevent the effects of sedimentation before spectral acquisitions.

Ligand exchange of Ag NCs. 50 nm Ag NCs stabilized with TSC as surface ligands were firstly synthesized in mass production with the method described previously. Typically, three aliquots of 50 mL each were purified by centrifugation (7000 rcf, 10 min). One of the aliquots was redispersed in the aqueous PVP solution (0.03 wt %) and stirred vigorously at room temperature for 3 h. Then, the resulting Ag NCs were washed again to eliminate the excess PVP and further redispersed in deionized water. Similarly, another of the aliquots was functionalized with the aqueous GEL solution (0.03 wt %) by the same procedure except that GEL was replaced by PVP as new surface ligands. For comparison, a third of the aliquots was redispersed in deionized water. Thus, three kinds of Ag NCs with different surface ligands (including TSC, PVP and GEL) were obtained and used as solution-based optical sensors for Hg^{2+} detection.

Structural characterization. The morphology, average size, and selected area electron diffraction pattern of Ag NCs were intuitively characterized by a JEOL transmission electron microscope (TEM, JEM-2100F), which was operated at an accelerating voltage of 200 kV. The average size and standard deviation in the size of all samples were obtained by statistically counting more than 100 particles according to their corresponding TEM images. Powder X-ray diffraction (XRD) was performed on the Rigaku SmartLab diffractometer with Cu K_α radiation

(λ=1.54056 Å). Fourier transform infrared (FT-IR) spectra were carried out on the PerkinElmer Frontier with the ATR accessory.

Figure S1. Schematic illustration of optical simulation based on Mie theory. (A) Calculated model of spherical Ag NCs dispersed in water with normal size distribution to predict the uniformity (standard deviation, 2-40 %) and nanoscale (average size, 30-220 nm) of the as-prepared Ag NCs. (B) Calculated spectra of spherical Ag NCs (10 %, 60 nm), the optical efficiencies including extinction, scattering, and absorption.

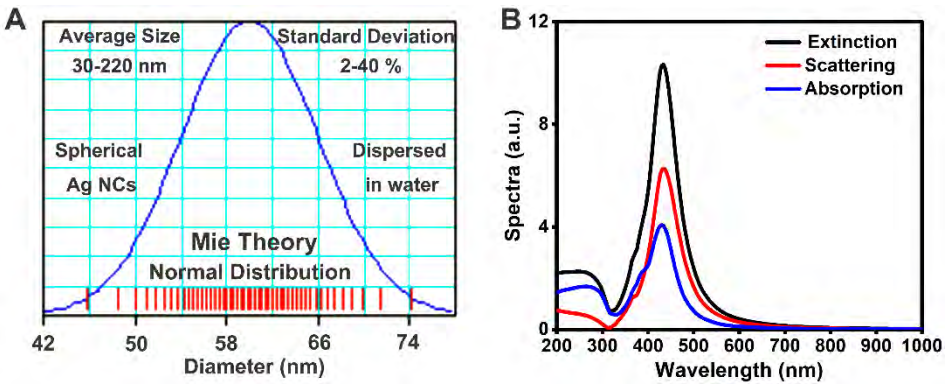

Figure S2. Schematic representations and physical images of the robotic platform.

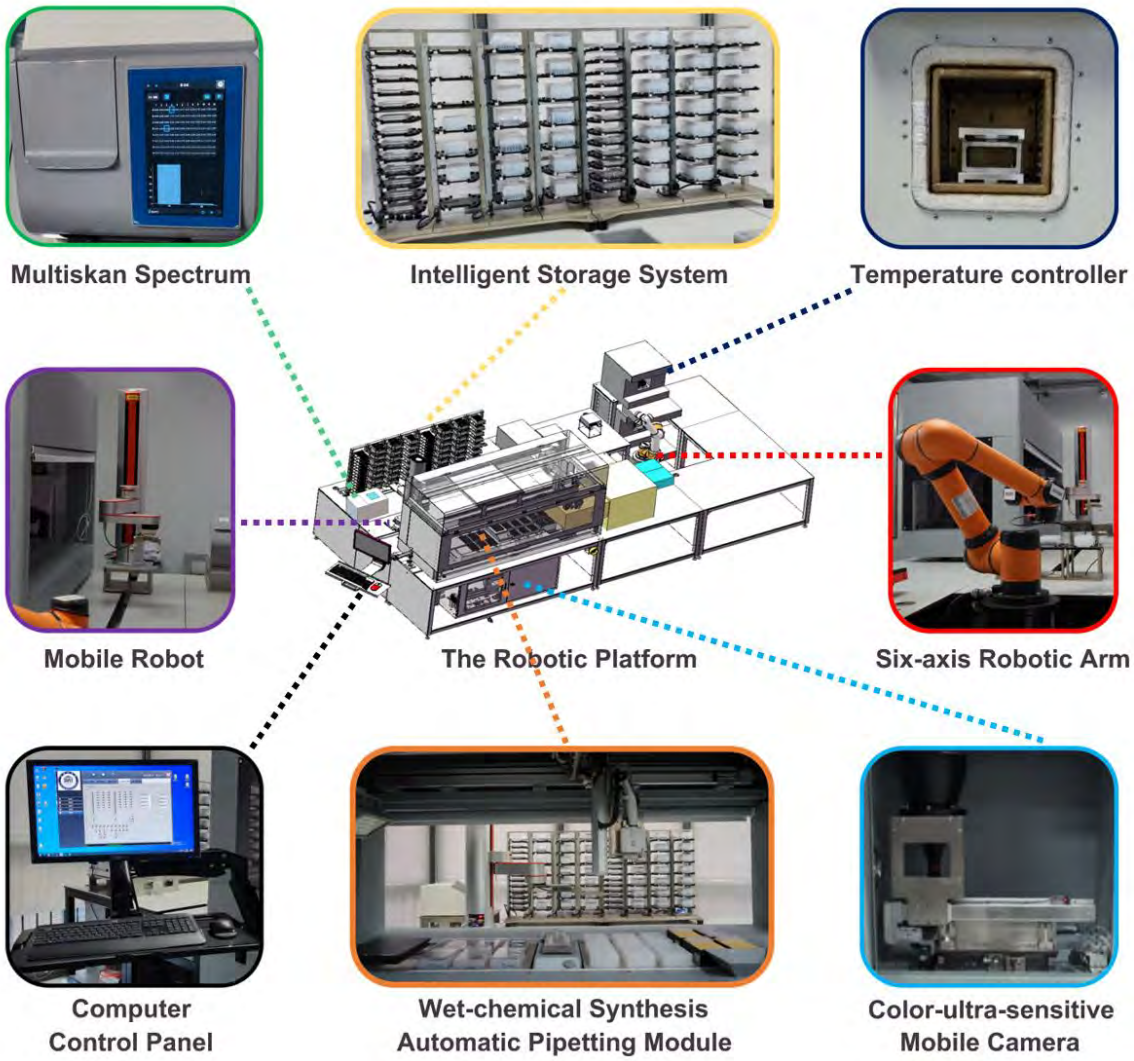

Figure S2 shows the structural model of the robotic platform and physical images of component parts. The robotic platform is equipped with a computer control panel for inputting experimental recipes and process steps, an automatic pipetting module with eight channels (1-1250 μL) and coordinate systems for liquid-phase high-throughput synthesis, a color-ultra-sensitive mobile camera for collecting the color change, a mobile robot carrying in a fixed trajectory for moving the samples to proper positions, a six-axis robotic arm transferring the samples to other devices for postprocessing, an intelligent storage system for storing the samples, a multiskan spectrum for bulk spectral acquisition, and a temperature controller for thermal demand. It can meet the needs of wet-chemical synthesis and *in situ* optical characterizations through the cooperation of various components on the automated platform.

Figure S3. Characterizations of Ag-NC seeds.

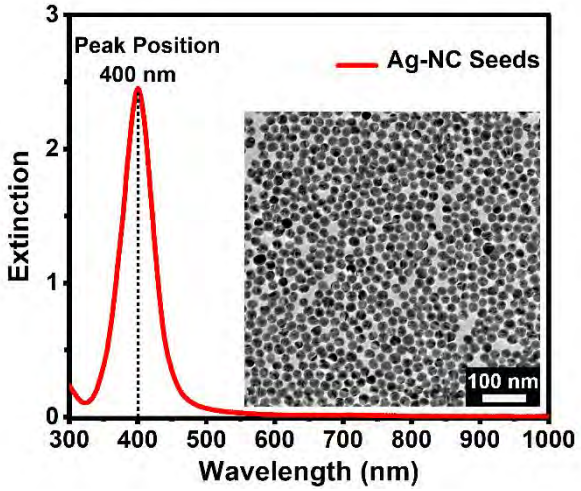

The Ag-NC seeds were first prepared according to the protocol described in the experimental section of Supporting Information. **Figure S3** shows the extinction spectrum and TEM image of Ag-NC seeds. The center position of the symmetrical peak in the extinction spectrum of Ag-NC seeds is at 400 nm. And the TEM result also shows that the Ag-NC seeds have a narrow size distribution and the average size is about 24 nm.

Figure S4. Extinction spectra of Ag NCs synthesized in 96 single-factor experiments. The single-factor experiments are carried out automatically on the robotic platform and grouped by the concentrations of various agents, including TSC (A, 0.03-2.88 mM), $NH_3 \cdot H_2O$ (B, 3-98 mM) and AA (C, 0.1-0.67 mM). For single-factor experiments, the values of other factors are fixed except for the investigated factor.

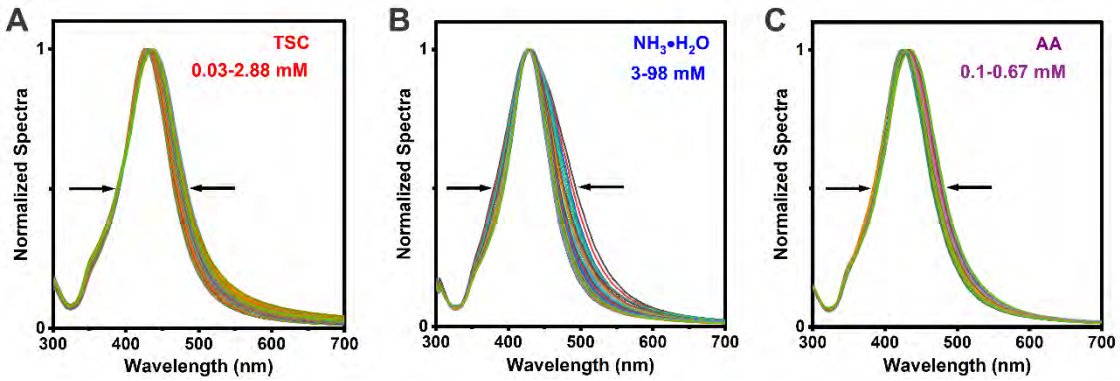

Figure S5. Experimental databases and ML models of FWHM for single-factor synthesis. (A-C) ML models with experimental databases of FWHM for single-factor synthesis, including TSC, $NH_3 \cdot H_2O$ and AA. (D-F) Scatter plots of the experimental value and ML predicted value for single-factor synthesis. The well-fitting responses (R^2>0.95) are obtained by ML algorithm of logistic regression.

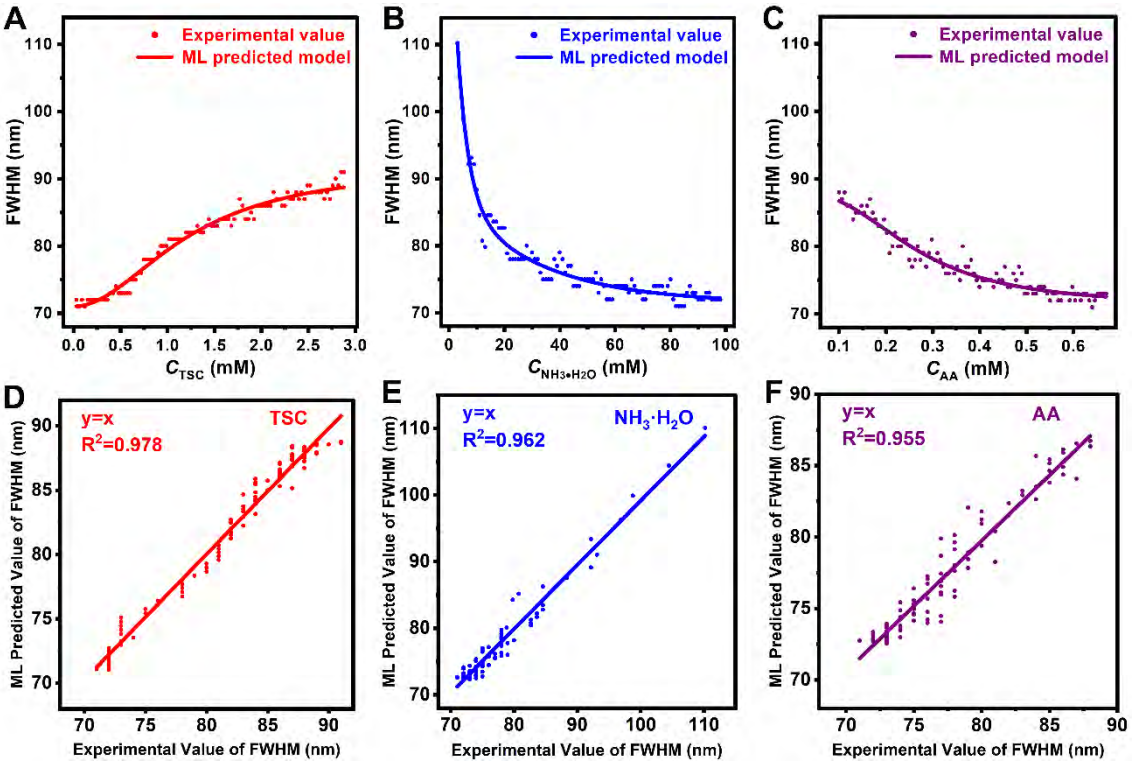

Figure S6. Extinction spectra of Ag NCs synthesized in 96 double-factor experiments grouped by the concentrations of TSC and $NH_3 \cdot H_2O$. For double-factor experiments, the values of other factors are fixed except for the investigated factors.

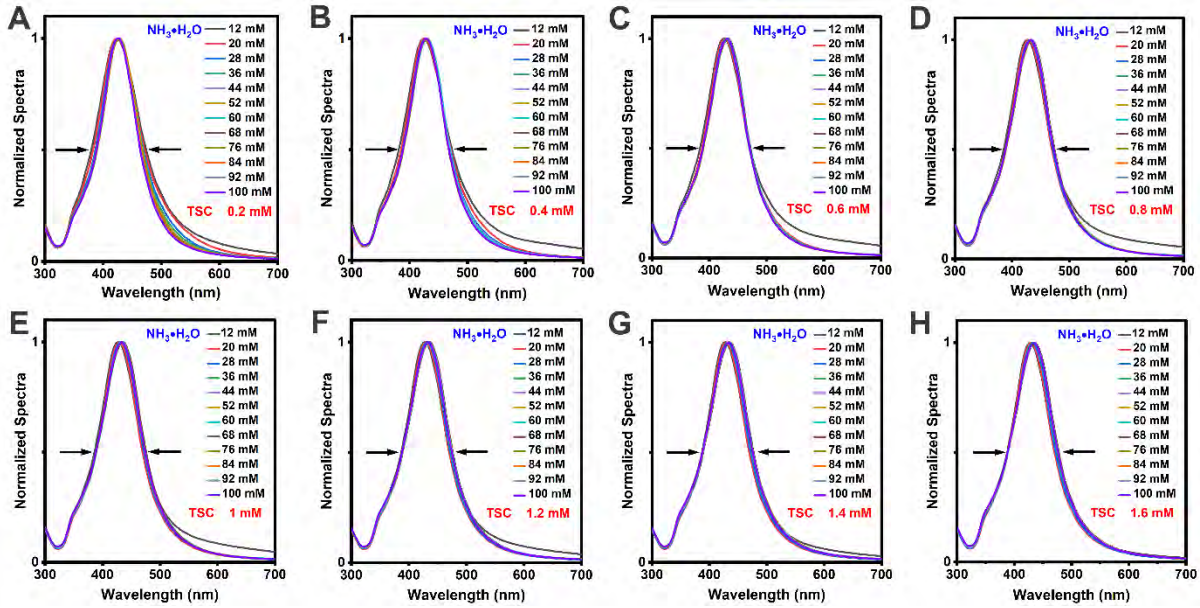

Figure S7. Extinction spectra of Ag NCs synthesized in 96 double-factor experiments grouped by the concentrations of TSC and AA. For double-factor experiments, the values of other factors are fixed except for the investigated factors.

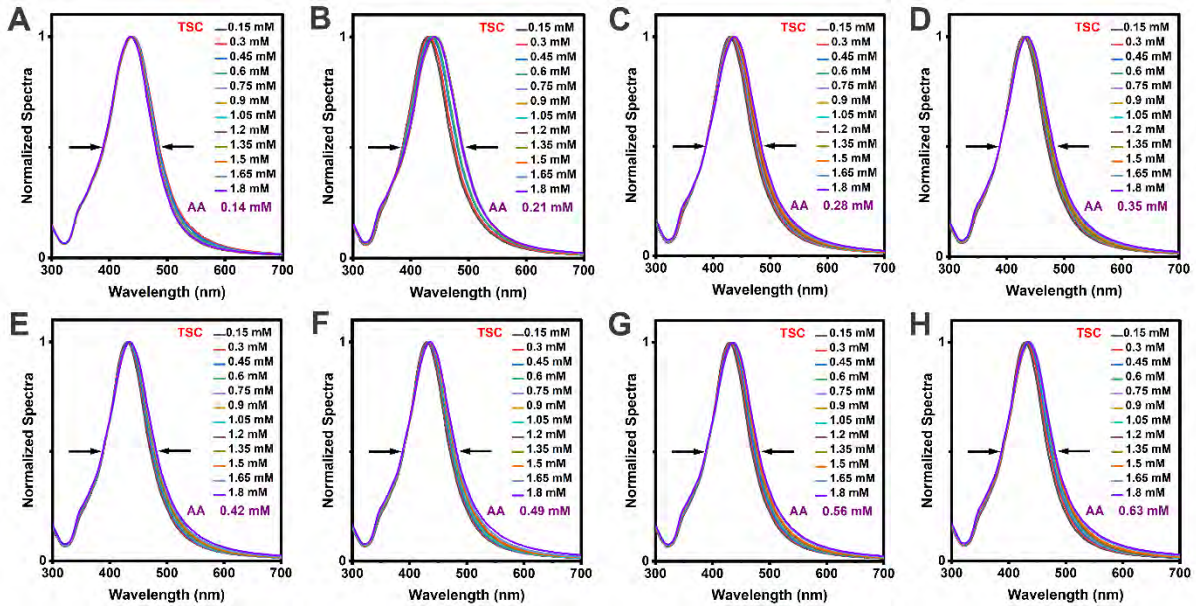

Figure S8. Extinction spectra of Ag NCs synthesized in 96 double-factor experiments grouped by the concentrations of $NH_3 \cdot H_2O$ and AA. For double-factor experiments, the values of other factors are fixed except for the investigated factors.

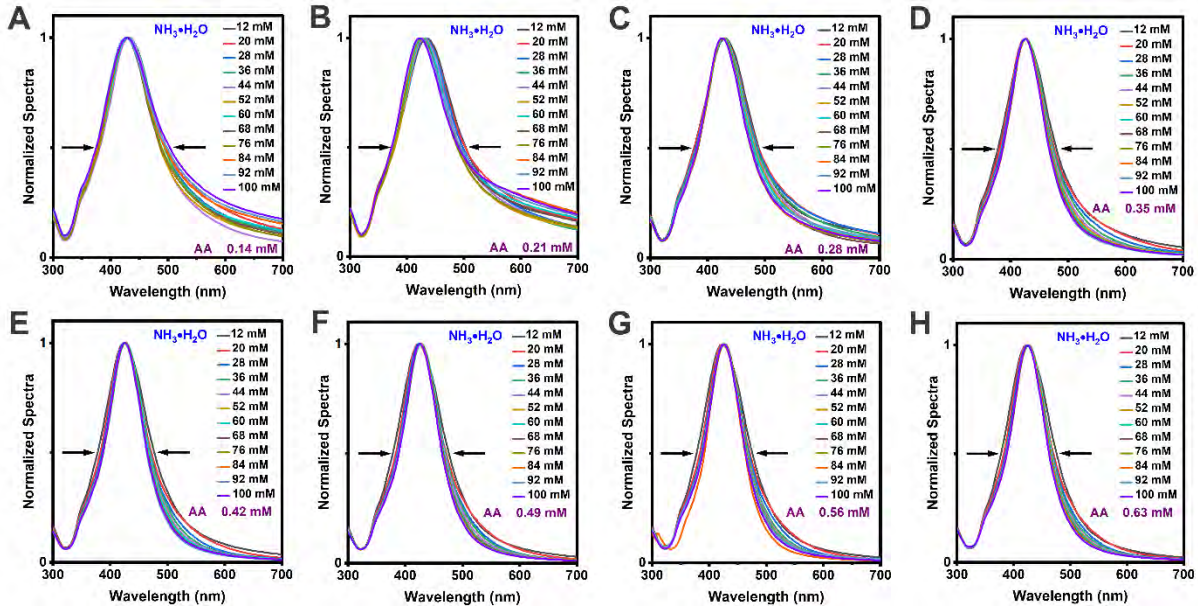

Figure S9. Experimental databases and ML models of FWHM for double-factor synthesis. (A-C) ML models with experimental databases of FWHM for double-factor synthesis, including TSC versus $NH_3 \cdot H_2O$, TSC versus AA, and $NH_3 \cdot H_2O$ versus AA. (D-F) Scatter plots of the experimental value and ML predicted value for double-factor synthesis. The well-fitting responses (R^2>0.96) are obtained by ML algorithm of SISSO.

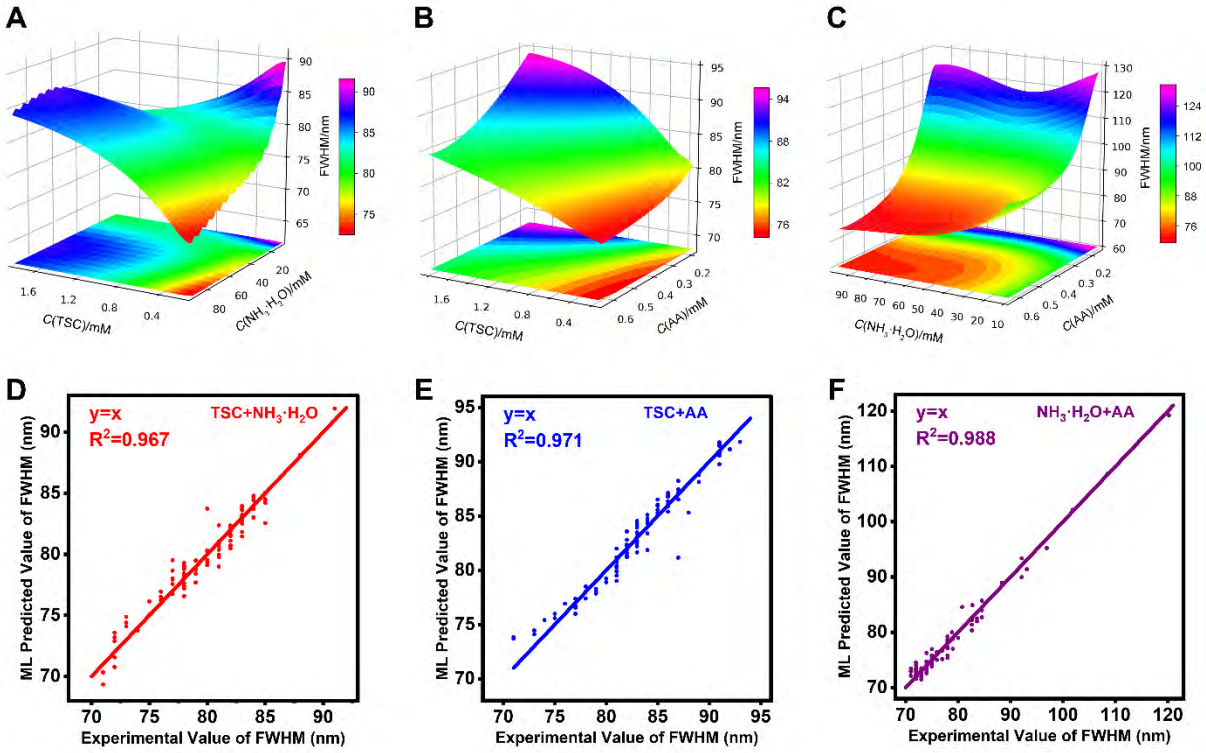

Figure S10. Experimental database and ML model of FWHM for triple-factor synthesis. (A) ML model with experimental database of FWHM for triple-factor synthesis, containing TSC, $NH_3 \cdot H_2O$ and AA. (B) Scatter plot of the experimental value and ML predicted value for triple-factor synthesis. The well-fitting response (R^2>0.97) is obtained by ML algorithm of SISSO.

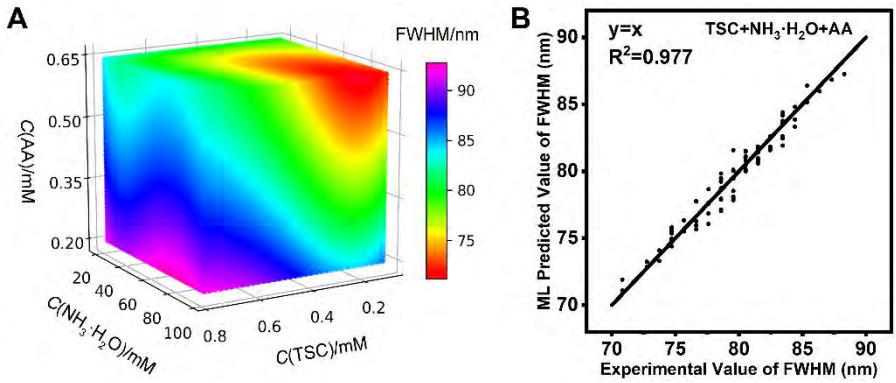

Figure S11. Overview of the high-throughput synthesis for the uniformity of Ag NCs. (A) Summarized data of the peak position of extinction spectra of the resulting Ag NCs obtained by the automated experiments on the robotic platform, including single factor, double factors and triple factors. (B) Summarized data of FWHM of extinction spectra of the resulting Ag NCs in the high-throughput synthesis for uniformity.

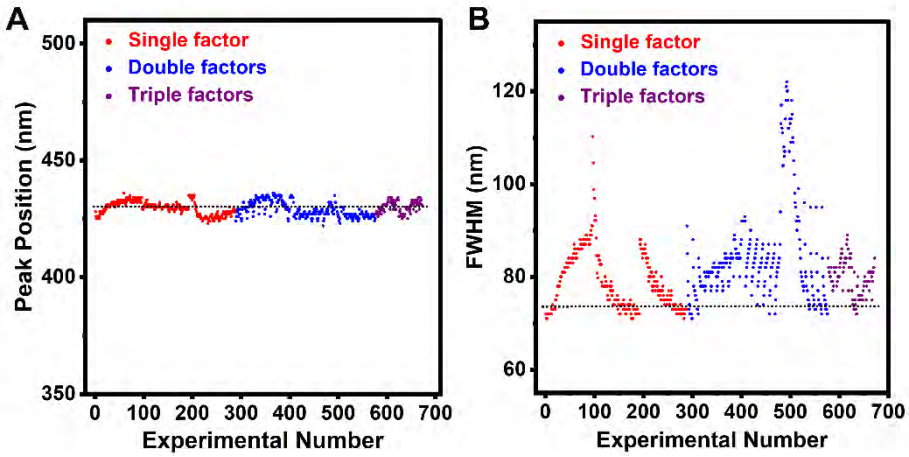

Figure S12. Redox potential analysis of the synthesis of Ag NCs.

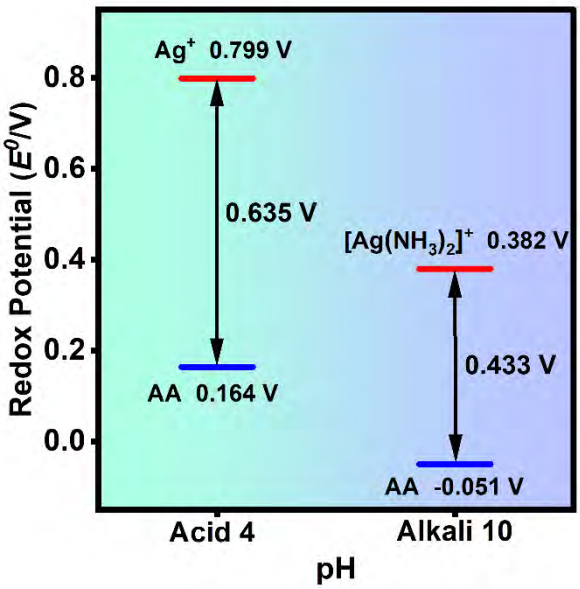

As shown in **Figure S12**, ammonia water plays an important role on the difference in redox potential in the seeded growth of Ag NCs. The difference in redox potential between $[Ag(NH_3)_2]^+$ and AA is about 0.433 V under the alkaline condition (pH=10), which is far lower that (0.635 V) between pure Ag^+ and AA under the acidic condition (pH=4). It can be clearly seen that the tendency of the Ag reduction is rather low after the addition of $NH_3 \cdot H_2O$, which results in fewer nuclei and slower growth of Ag layers on Ag-NC seeds.

Figure S13. Kinetic analysis of the synthesis of Ag NCs.

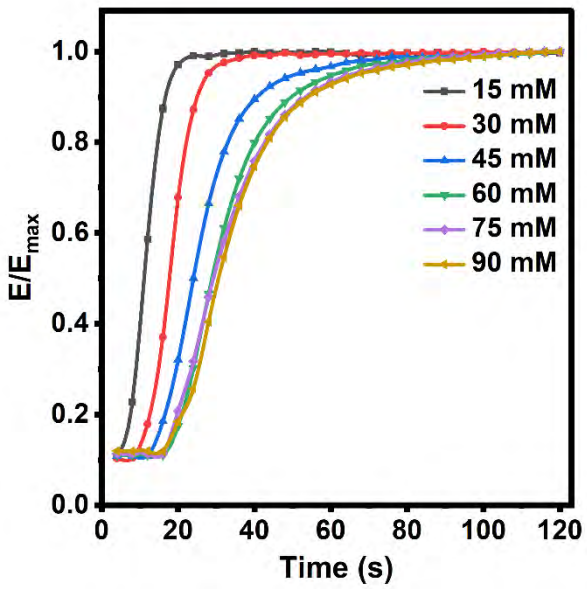

Figure S13 shows the kinetic curves of Ag NCs during the seeded growth with different concentrations of $NH_3 \cdot H_2O$ by plotting the variation (E/E_{max}) of the dipolar peak intensity in extinction spectra. For dynamic experiments, the values of other factors are fixed as shown in **Table S2** except for the concentration of $NH_3 \cdot H_2O$. The results indicate that the concentration of $NH_3 \cdot H_2O$ can regulate the growth rate of Ag NCs, which should be finely adjusted.

Figure S14. The reproducibility of the established ML model for the uniformity of synthesis. (A-C) Extinction spectra of the resulting Ag NCs obtained by regularly changing the particle number of seeds under different optimal conditions (given in **Figure 2C** and **Table S5**). (D) Scatter diagram of FWHM of the dipolar peak in extinction spectra. (E) Scatter diagram of the dipolar peak position in extinction spectra. (F) Scatter diagram of the actual diameter of the resulting Ag NCs based on the dipolar peak position and the ML predicted model (**Figure 2E**).

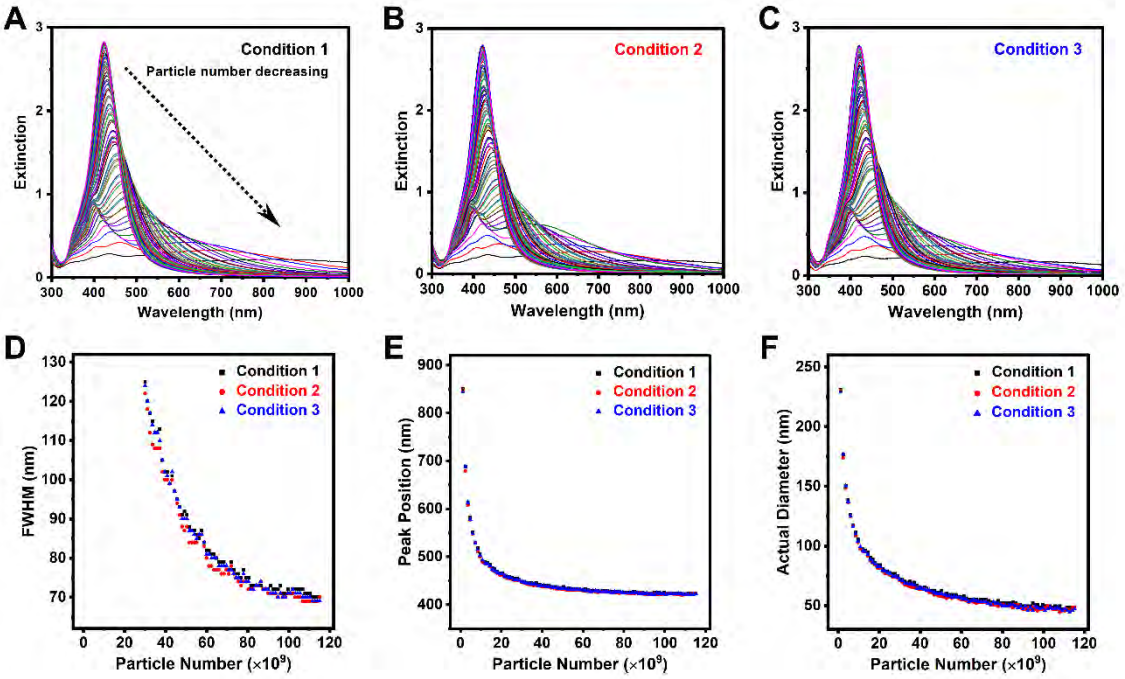

Figure S15. Relationship between the diameter of Ag NCs and the particle number of seeds. (A-C) Synthetic databases and the classical growth models between the diameter of Ag NCs and the particle number of seeds under different optimal conditions. (D-F) Scatter plots of the actual diameter based on the ML model of optical simulation and the calculated diameter based on the classical growth model. The well-fitting responses of experimental results (R^2>0.99) are obtained by the classical growth model.

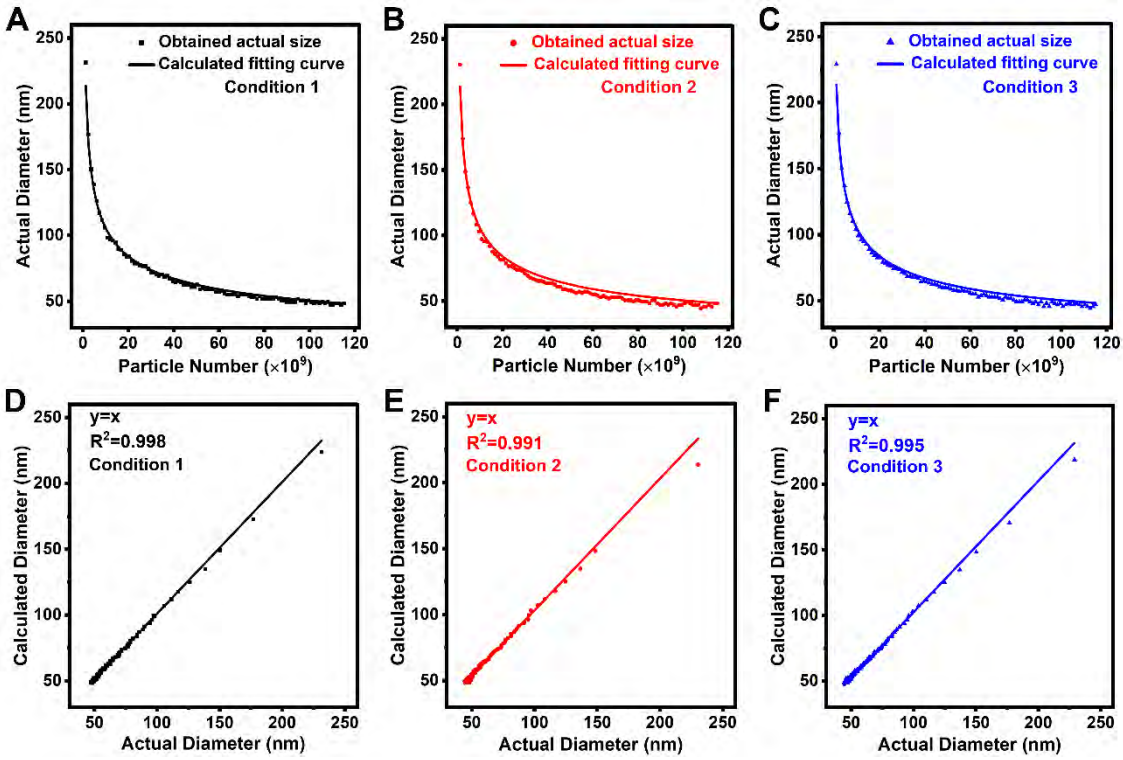

Figure S16. Size control of Ag NCs with regular intervals. (A) Relationship between the actual diameter of Ag NCs and the particle number of seeds based on the classical growth model. (B) Linear curve by plotting the actual diameter of Ag NCs (D) with the reciprocal of the cube root of the particle number of seeds ($N^{-1/3}$). The well-fitting response (R^2>0.99) is obtained by ML algorithm of linear regression.

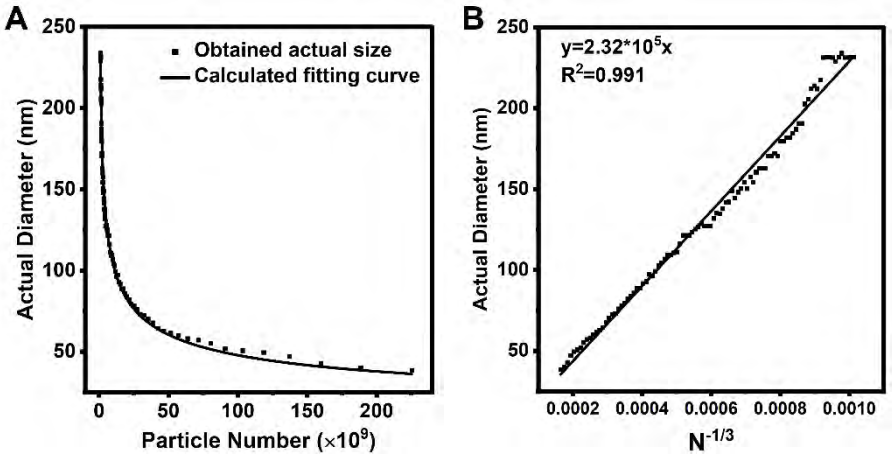

Figure S17. RGB colors of Ag NCs with size control. (A) Color database with ML model of RGB value and the Ag-NC size. The concentration of Ag atom is fixed at 0.4 mM in this system. (B) Scatter plot of the actual size and ML predicted size of Ag NCs. The well-fitting response (R^2>0.99) is obtained by ML algorithm of SISSO.

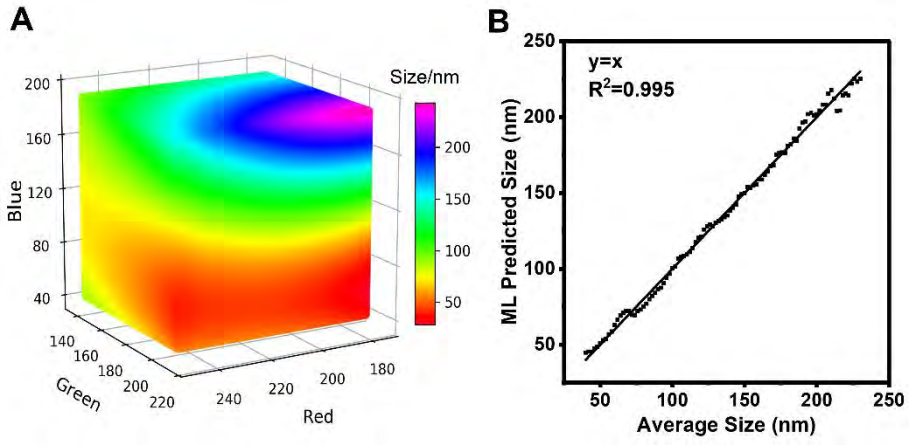

Figure S18. Statistical chart of the actual size of Ag NCs obtained in scale-up experiments.

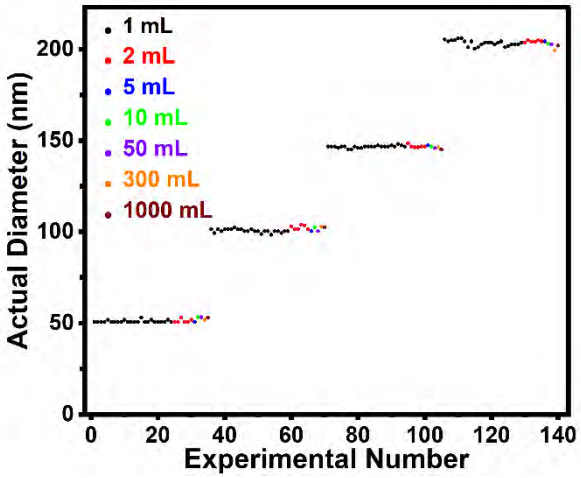

Figure S18 shows the actual size of Ag NCs obtained in scale-up experiments. It can be clearly seen that the actual diameters of Ag NCs obtained in different volumes are almost the same, which indicates that the optimal recipes screened on the robotic platform can be perfectly repeated to meet the imperious demand of the mass production of Ag NCs with high quality for many practical applications.

Figure S19. Low-magnification TEM images (A-D) of Ag NCs synthesized in mass productions with various sizes (50, 100, 150, and 200 nm).

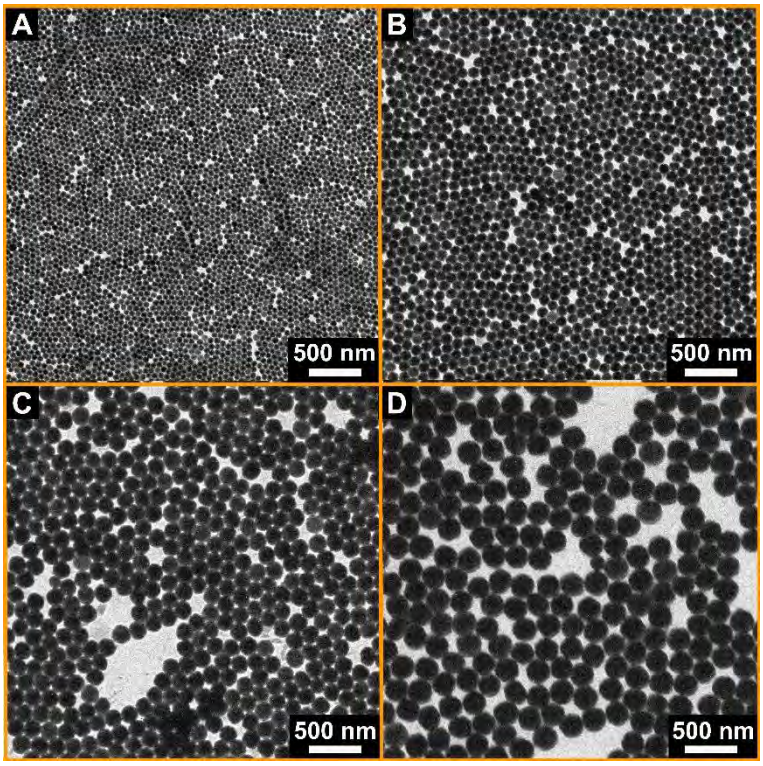

Figure S20. Long-term stability of Ag NCs with different sizes synthesized in mass production. (A) Extinction spectra of 50 nm Ag NCs after fresh synthesis and storage for 6 weeks. (B) Extinction spectra of 100 nm Ag NCs after fresh synthesis and storage for 6 weeks. (C) Extinction spectra of 150 nm Ag NCs after fresh synthesis and storage for 6 weeks. (D) Extinction spectra of 200 nm Ag NCs after fresh synthesis and storage for 6 weeks.

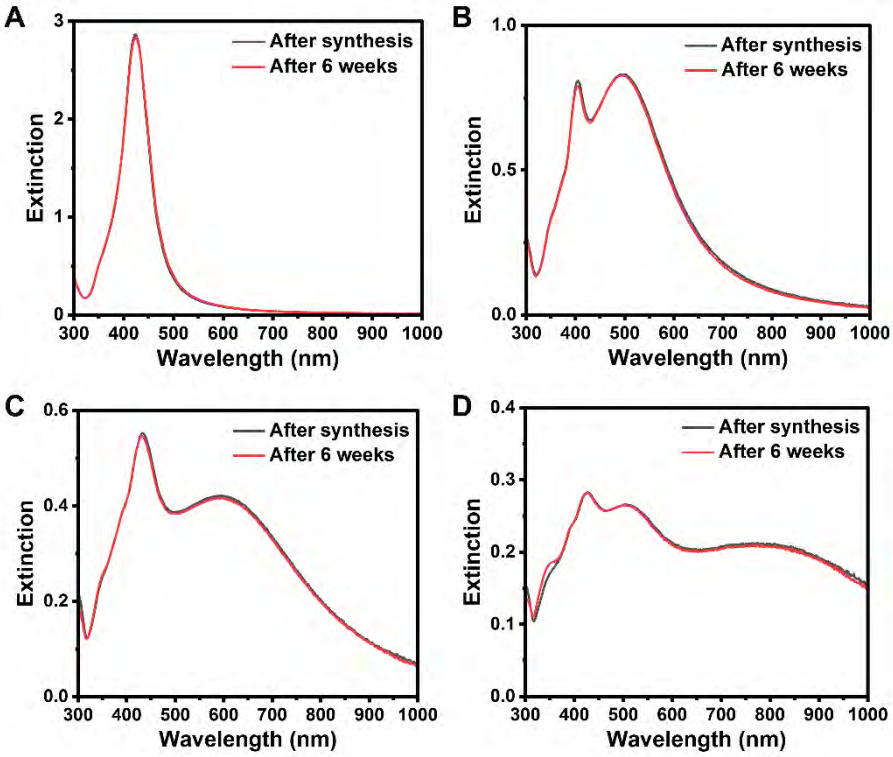

Figure S21. Selective identification of Hg^{2+}. (A) Extinction spectra of 50 nm Ag NCs before and after the addition of various metal ions, including Na^{+}, K^{+}, Li^{+}, Mg^{2+}, Ca^{2+}, Zn^{2+}, Al^{3+}, Fe^{2+}, Fe^{3+}, Co^{2+}, Ni^{2+}, Ti^{4+}, Cu^{2+}, Cd^{2+}, Cr^{3+}, Mn^{2+}, Sr^{2+}, Zr^{4+}, Ag^{+}, Ba^{2+}, Pb^{2+}, Ga^{3+}, and Hg^{2+}. The final concentrations of various metal ions in aqueous solutions are fixed at 0.2 mM. (B) High-quality digital photo of 50 nm Ag NCs before and after the addition of various metal ions. (C) Recognized RGB color-block photo generated from the corresponding digital photo.

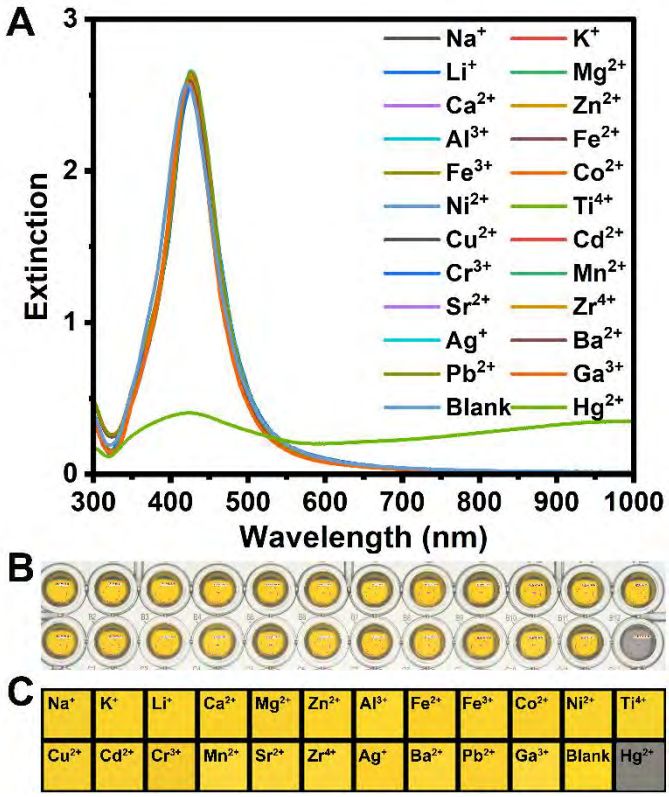

Figure S22. XRD patterns of Ag NCs before and after the addition of Hg^{2+} (10 μM).

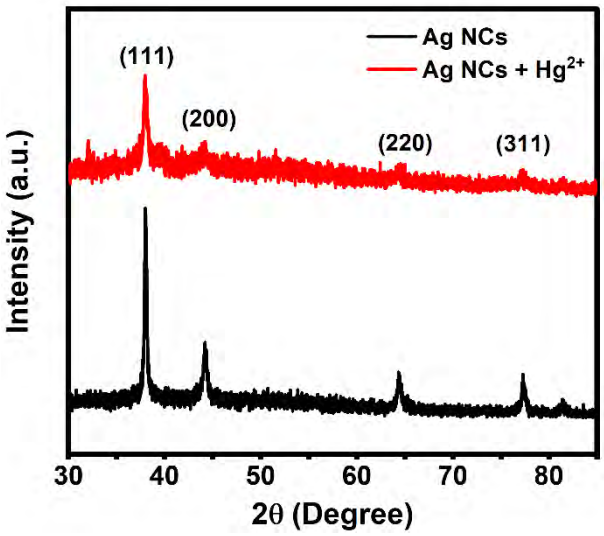

Figure S23. FT-IR spectra of Ag NCs modified with various ligands. (A) FT-IR spectra of TSC-Ag NCs and TSC. (B) FT-IR spectra of PVP-Ag NCs and PVP. (C) FT-IR spectra of GEL-Ag NCs and GEL.

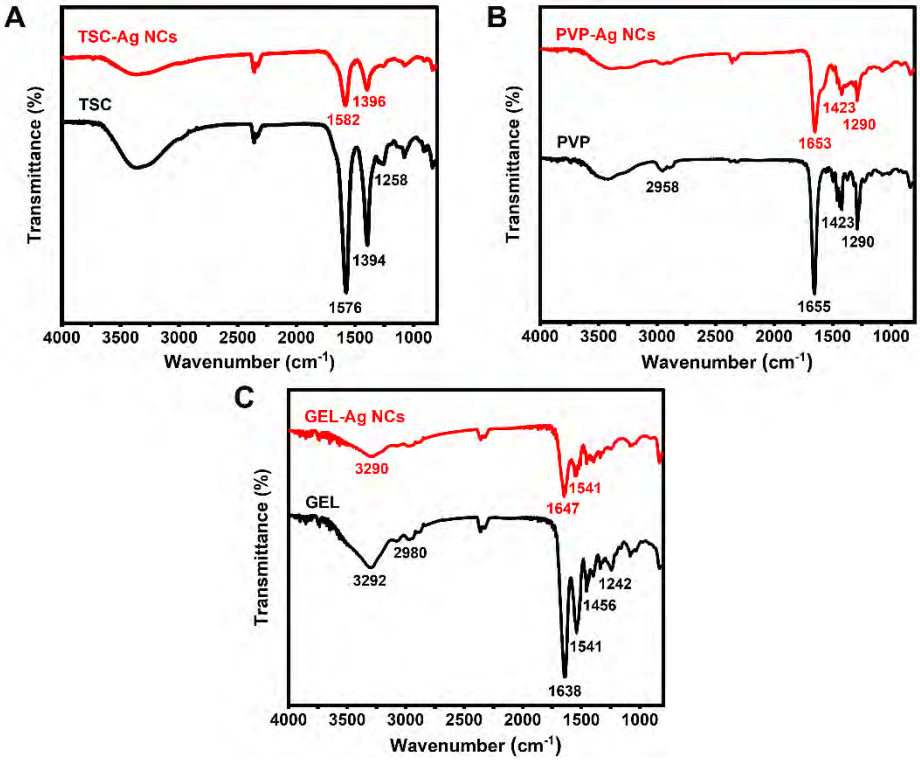

As shown in **Figure S23**, FT-IR analysis is used to characterize the functional groups and structural bonds of chemical substances on the surface of Ag NCs. Two strong peaks corresponding to the stretching modes of the carboxylic group of TSC are located at 1394 cm^{-1} and 1576 cm^{-1} in the FT-IR spectrum (**Figure S23A**). And the peak positions of TSC-Ag NCs shift slightly to 1396 cm^{-1} and 1582 cm^{-1} in the FT-IR spectrum. Compared with the strong peaks of PVP, the typical bands of the C-N and C=O of PVP-Ag NCs at 1290 cm^{-1} and 1653 cm^{-1} are reduced remarkably (**Figure S23B**). The result indicates that PVP ligands successfully replace TSC ligands and combine with Ag NCs through the C-N and C=O bands. Three obvious characteristic peaks corresponding to amide Ⅰ, Ⅱ, and Ⅲ of GEL are located at 1638 cm^{-1}, 1541 cm^{-1}, and 1242 cm^{-1} (**Figure S23C**), which can be attributed to the presence of the C=O stretching vibration, the N-H bending vibration, and the N-H stretching vibration. In the FT-IR spectrum of GEL-Ag NCs, the band of the C=O stretching vibration shifts to 1647 cm^{-1} and the band of the N-H stretching vibration almost disappears, indicating GEL ligands successfully bind to the surface of Ag NCs. These results validate that TSC-Ag NCs are successfully modified with PVP and GEL through ligand exchange.

Figure S24. Differences in Hg^{2+} detection of Ag NCs modified with different surface ligands. (A) Extinction spectra of 50 nm TSC-Ag NCs before and after the addition of Hg^{2+}. (B) Extinction spectra of 50 nm PVP-Ag NCs before and after the addition of Hg^{2+}. (C) Extinction spectra of 50 nm GEL-Ag NCs before and after the addition of Hg^{2+}. The final concentration of Hg^{2+} in aqueous solutions is fixed at 0.2 mM.

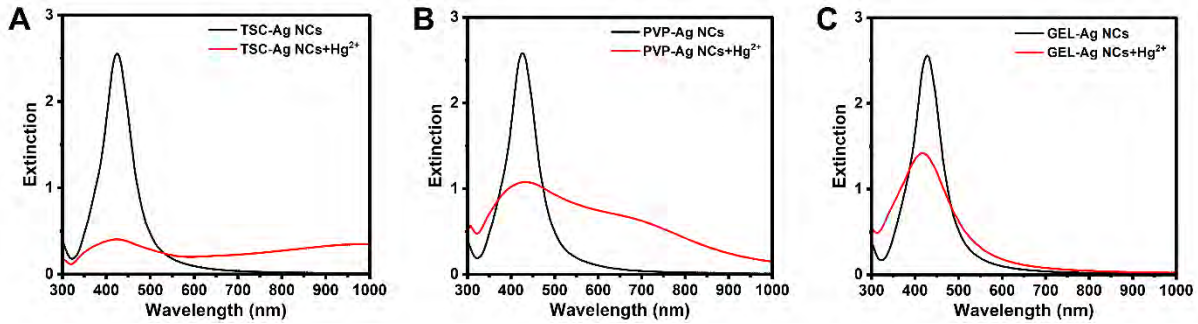

Figure S25. Color changes of Hg^{2+} detection. (A) High-quality digital photo of 50 nm Ag NCs modified with different ligands after the addition of different concentrations of Hg^{2+} (0-200 μM). (B) Recognized RGB color-block photo generated from the corresponding digital photo. Each test is carried out three times in parallel on the platform.

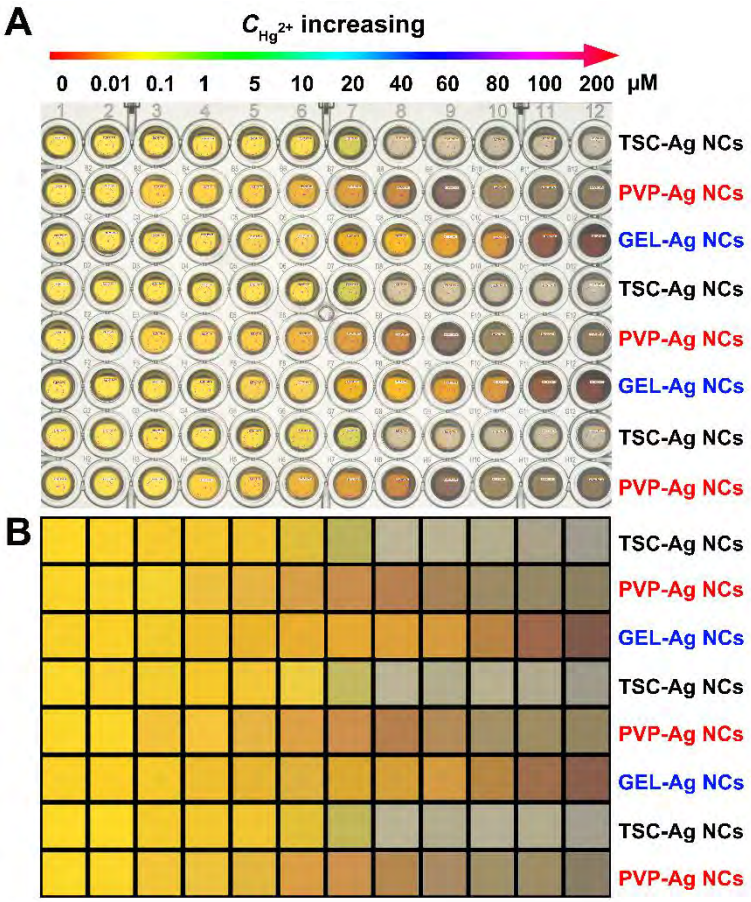

Figure S26. Hg^{2+} detection of Ag NCs modified with various surface ligands. (A-C) Extinction spectra of 50 nm Ag NCs with different concentrations of Hg^{2+} (0-200 μM). The surfaces of Ag NCs are modified by TSC, PVP and GEL, respectively. (D-F) Scatter diagrams of the changing ratio ($\Delta E/E_{max}$) of extinction value of dipolar peaks with the corresponding concentrations of Hg^{2+}. The error bars are added from the results of three parallel experiments.

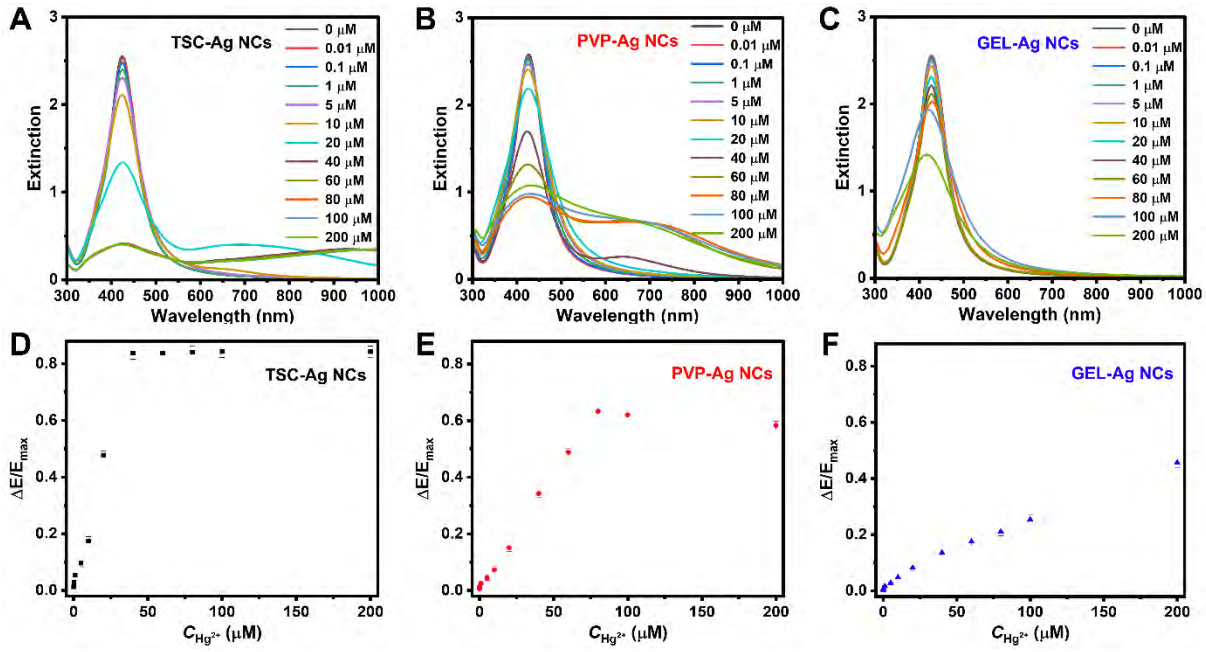

Figure S27. Interference study of the synthesized Ag NCs as optical sensors in real water samples. (A-C) Histograms of the changing ratios ($\Delta E/E_{max}$) of extinction intensities of TSC-Ag NCs (A), PVP-Ag NCs (B), and GEL-Ag NCs (C) after the addition of different metal ions (0.2 mM).

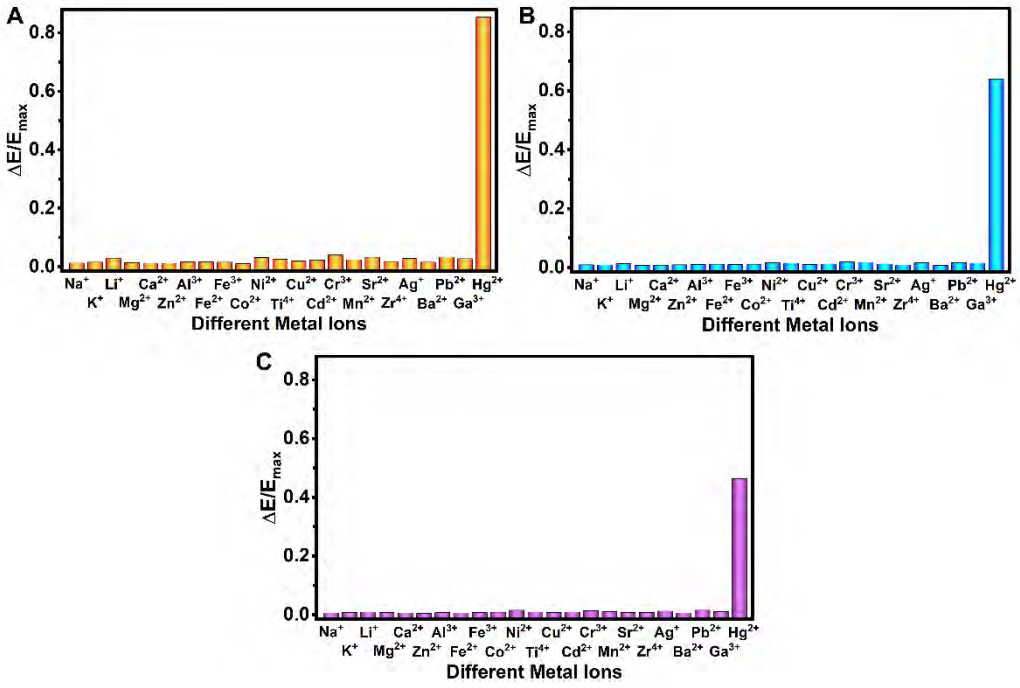

Table S1. Database of optical simulation of Ag NCs. Extinction spectra of spherical Ag NCs generally with normal distributions were simulated to predict the uniformity and nanoscale of the as-prepared Ag NCs as targeted data screening (**Figure 2A and 2D**).

Uniformity					Nanoscale				
No.	Size [a] (nm)	SD [b] (%)	FWHM [c] (nm)	Peak [d] (nm)	No.	Size (nm)	SD (%)	FWHM (nm)	Peak (nm)
1	60	2	69	434	21	30	10	38	406
2	60	4	70	434	22	40	10	46	413
3	60	6	71	433	23	50	10	58	423
4	60	8	72	433	24	60	10	73	432
5	60	10	73	432	25	70	10	100	446
6	60	12	75	432	26	80	10	134	462
7	60	14	76	431	27	90	10	/ [e]	475
8	60	16	78	431	28	100	10	/	496
9	60	18	80	430	29	110	10	/	514
10	60	20	82	430	30	120	10	/	537
11	60	22	84	428	31	130	10	/	561
12	60	24	85	428	32	140	10	/	585
13	60	26	87	428	33	150	10	/	612
14	60	28	88	427	34	160	10	/	636
15	60	30	90	427	35	170	10	/	666
16	60	32	91	426	36	180	10	/	697
17	60	34	92	426	37	190	10	/	727
18	60	36	93	425	38	200	10	/	757
19	60	38	94	425	39	210	10	/	786
20	60	40	95	424	40	220	10	/	817

[a] The average size of Ag NCs is equal to the average diameter (D) of Ag NCs. [b] The standard deviation (SD) of the size follows the normal distribution. [c] The full width at half maxima (FWHM) is estimated from the width at half of the dipolar peak of the simulated spectra. [d] The center position of the dipolar peak is measured from the simulated spectra.

Table S2. Summarized recipes of single-factor experiments for the uniformity of synthesis. For single-factor experiments, the values of other factors were fixed as standard values except for the investigated factor. The single-factor experiments with 96 concentration gradients were carried out with regular intervals. And the standard values of the concentrations of TSC, $NH_3 \cdot H_2O$ and AA were 0.15, 90 and 0.65 mM, respectively. The amounts of silver precursors including seeds and $AgNO_3$ were fixed.

No.	N_{Seeds} ($\times 10^{10}$)	$AgNO_3$ (mM)	TSC (mM)	$NH_3 \cdot H_2O$ (mM)	AA (mM)
1	5.83	0.4	0.03	3	0.100
2			0.06	4	0.106
3			0.09	5	0.112
4			0.12	6	0.118
5			0.15	7	0.124
6			0.18	8	0.130
7			0.21	9	0.136
8			0.24	10	0.142
9			0.27	11	0.148
10			0.30	12	0.154
11			0.33	13	0.160
12			0.36	14	0.166
…			…	…	…
96			2.88	98	0.670
Range	Fixed	Fixed	0.03-2.88	3-98	0.1-0.67
Interval	0	0	0.03	1	0.006

Table S3. Summarized recipes of double-factor experiments for the uniformity of synthesis. For double-factor experiments, the values of other factors were fixed as standard values except for the investigated factors. The double-factor experiments with 96 concentration gradients were carried out with 8 × 12 levels. And the fixed standard values of TSC, $NH_3 \cdot H_2O$, AA, seeds and $AgNO_3$ were shown in **Table S2**.

TSC versus $NH_3 \cdot H_2O$			TSC versus AA			$NH_3 \cdot H_2O$ versus AA		
Level	TSC (mM)	$NH_3 \cdot H_2O$ (mM)	Level	TSC (mM)	AA (mM)	Level	$NH_3 \cdot H_2O$ (mM)	AA (mM)
1	0.2	12	1	0.15	0.14	1	12	0.14
2	0.4	20	2	0.30	0.21	2	20	0.21
3	0.6	28	3	0.45	0.28	3	28	0.28
4	0.8	36	4	0.60	0.35	4	36	0.35
5	1.0	44	5	0.75	0.42	5	44	0.42
6	1.2	52	6	0.90	0.49	6	52	0.49
7	1.4	60	7	1.05	0.56	7	60	0.56
8	1.6	68	8	1.20	0.63	8	68	0.63
9		76	9	1.35		9	76	
10		84	10	1.50		10	84	
11		92	11	1.65		11	92	
12		100	12	1.80		12	100	

Table S4. Summarized recipes of triple-factor experiments for the uniformity of synthesis. The triple-factor experiments with 96 concentration gradients were carried out with 4 × 6 × 4 levels. And the fixed standard values of seeds and $AgNO_3$ were shown in **Table S2**.

Level	Triple-factor experiments		
	TSC (mM)	$NH_3 \cdot H_2O$ (mM)	AA (mM)
1	0.2	15	0.2
2	0.4	30	0.35
3	0.6	45	0.50
4	0.8	60	0.65
5		75	
6		90	

Table S5. Summarized recipes of confirmatory experiments for the uniformity of synthesis. The optimized conditions for the uniformity of synthesis were given by the established ML model (**Figure 2C**) of multiple synthesis factors.

No.	N_{Seeds} ($\times 10^{10}$)	Condition 1	No.	N_{Seeds} ($\times 10^{10}$)	Condition 2	No.	N_{Seeds} ($\times 10^{10}$)	Condition 3
1	0.12	$AgNO_3$ (0.4 mM) + TSC (0.15 mM) + $NH_3 \cdot H_2O$ (95 mM) + AA (0.55 mM)	97	0.12	$AgNO_3$ (0.4 mM) + TSC (0.2 mM) + $NH_3 \cdot H_2O$ (90 mM) + AA (0.6 mM)	193	0.12	$AgNO_3$ (0.4 mM) + TSC (0.25 mM) + $NH_3 \cdot H_2O$ (85 mM) + AA (0.65 mM)
2	0.24		98	0.24		194	0.24	
3	0.36		99	0.36		195	0.36	
4	0.48		100	0.48		196	0.48	
5	0.60		101	0.60		197	0.60	
6	0.72		102	0.72		198	0.72	
7	0.84		103	0.84		199	0.84	
8	0.96		104	0.96		200	0.96	
9	1.08		105	1.08		201	1.08	
10	1.20		106	1.20		202	1.20	
11	1.32		107	1.32		203	1.32	
12	1.44		108	1.44		204	1.44	
…	…		…	…		…	…	
96	11.52		192	11.52		288	11.52	
Range	0.12-11.52	Fixed	Range	0.12-11.52	Fixed	Range	0.12-11.52	Fixed
Interval	0.12	0	Interval	0.12	0	Interval	0.12	0

Table S6. Summarized recipes of size-control experiments. For size-control experiments, the required particle number of Ag-NC seeds (N_{Seeds}) could be calculated according to the classical growth model. The calculated diameter (Cal. D) of Ag NCs were set in the range of 40 to 230 nm with regular interval. And the concentrations of $AgNO_3$, TSC, $NH_3 \cdot H_2O$ and AA were 0.4, 0.15, 90 and 0.65 mM, respectively.

No.	Cal. D (nm)	N_{Seeds} ($\times 10^{10}$)	No.	Cal. D (nm)	N_{Seeds} ($\times 10^{10}$)	No.	Cal. D (nm)	N_{Seeds} ($\times 10^{10}$)
1	40	23.485	33	104	1.061	65	168	0.249
2	42	19.553	34	106	1.001	66	170	0.241
3	44	16.513	35	108	0.946	67	172	0.232
4	46	14.110	36	110	0.895	68	174	0.224
5	48	12.177	37	112	0.847	69	176	0.217
6	50	10.599	38	114	0.803	70	178	0.209
7	52	9.294	39	116	0.762	71	180	0.203
8	54	8.204	40	118	0.723	72	182	0.196
9	56	7.283	41	120	0.687	73	184	0.190
10	58	6.500	42	122	0.654	74	186	0.184
11	60	5.828	43	124	0.623	75	188	0.178
12	62	5.249	44	126	0.593	76	190	0.172
13	64	4.745	45	128	0.566	77	192	0.167
14	66	4.306	46	130	0.540	78	194	0.162
15	68	3.920	47	132	0.515	79	196	0.157
16	70	3.580	48	134	0.493	80	198	0.152
17	72	3.278	49	136	0.471	81	200	0.148
18	74	3.011	50	138	0.451	82	202	0.143
19	76	2.772	51	140	0.432	83	204	0.139
20	78	2.558	52	142	0.414	84	206	0.135
21	80	2.365	53	144	0.396	85	208	0.131
22	82	2.192	54	146	0.380	86	210	0.127
23	84	2.036	55	148	0.365	87	212	0.124
24	86	1.894	56	150	0.351	88	214	0.120
25	88	1.765	57	152	0.337	89	216	0.117
26	90	1.648	58	154	0.324	90	218	0.114
27	92	1.541	59	156	0.312	91	220	0.111
28	94	1.443	60	158	0.300	92	222	0.108
29	96	1.353	61	160	0.289	93	224	0.105
30	98	1.271	62	162	0.278	94	226	0.102
31	100	1.195	63	164	0.268	95	228	0.100
32	102	1.125	64	166	0.258	96	230	0.097

Table S7. Summarized ML models of FWHM for the uniformity of synthesis.

Factor (Concentration, mM)		Training Dataset	ML Algorithm	R^2	RMSE	MaxAE
Single	TSC (x)	96	Logistic Regression	0.978	/	/
		ML model: $92-21/[1+(x/1.23)^{1.98}]$				
	$NH_3 \cdot H_2O$ (y)	96	Logistic Regression	0.962	/	/
		ML model: $71+39/[1+(y/8.22)^{1.32}]$				
	AA (z)	96	Logistic Regression	0.955	/	/
		ML model: $71+17/[1+(z/0.26)^{2.59}]$				
Double	x + y	96	SISSO [a]	0.967	1.001	3.729
		ML model: $-6.1[sin(lnx)sin(lny)]-3.1[sin(lny)lnx/e^{x}]+1.4[sin(y^{1/2})-siny/lny]+81.3$				
	x + z	96	SISSO	0.971	1.119	5.846
		ML model: $-9.1[cos(x^{1/3}/z^{1/2})]+0.5[cos(z^{-1})sinx/sinz]+22.8(z^{9}x^{2}/sinx)+82.8$				
	y + z	96	SISSO	0.988	2.715	8.381
		ML model: $-42.8[(zlny)^{1/2}]-12.9[cos(z^{-1})/lnz]-1.1[(y/z)cos(y^{1/2})]+145.9$				
Triple	x + y + z	96	SISSO	0.977	1.176	3.104
		ML model: $1.8[(sinz)^{-1}+sinxlny]-143.5[sin(y^{1/3})lnxz/y]+1.2[cos(xy^{1/3})]+72.2$				

[a] The SISSO models work in a hierarchical order, which creates a new feature space of varying complexity through algebraic operations (+ , -, ×, /, *sin*, *cos*, $()^{1/2}$, $()^{-1}$, $()^{2}$, $()^{3}$, e^{x}, *ln*) on primary feature sets.

Table S8. Summarized data of extinction spectra of Ag NCs with size control.

Cal. D [a] (nm)	SPR peak (nm) [b]		Act. D [c] (nm)	Cal. D (nm)	SPR peak (nm)		Act. D (nm)	Cal. D (nm)	SPR peak (nm)			Act. D (nm)
	Dipo.	Quadru.			Dipo.	Quadru.			Dipo.	Quadru.	Oct.	
40	416	/	38.4	104	503	408	104.4	168	648	449	/	162.9
42	417	/	40.0	106	508	410	106.8	170	648	452	/	162.9
44	419	/	43.0	108	513	411	109.2	172	648	453	/	162.9
46	422	/	47.0	110	513	412	109.2	174	670	458	412	170.6
48	424	/	49.5	112	516	412	110.6	176	670	465	414	170.6
50	425	/	50.6	114	517	414	111.1	178	674	462	414	172.0
52	426	/	51.8	116	528	416	116.2	180	670	462	413	170.6
54	429	/	55.0	118	540	419	121.4	182	696	463	414	179.5
56	431	/	57.0	120	540	418	121.4	184	696	463	414	179.5
58	432	/	58.0	122	540	420	121.4	186	703	471	414	181.9
60	434	/	59.9	124	545	421	123.6	188	703	476	420	181.9
62	436	/	61.8	126	549	421	125.3	190	711	484	421	184.6
64	437	/	62.7	128	552	421	126.5	192	718	492	425	186.9
66	439	/	64.4	130	557	424	128.6	194	729	492	425	190.6
68	443	/	67.7	132	554	424	127.4	196	729	508	437	190.6
70	446	/	70.1	134	554	424	127.4	198	765	500	430	202.6
72	449	/	72.4	136	554	425	127.4	200	774	502	432	205.6
74	450	/	73.1	138	565	427	131.8	202	794	502	437	212.3
76	454	/	76.0	140	573	427	135.0	204	799	500	437	213.9
78	457	/	78.0	142	572	429	134.7	206	793	503	440	211.9
80	459	/	79.4	144	580	430	137.8	208	810	515	440	217.6
82	463	400	82.0	146	590	432	141.7	210	851	525	444	231.3
84	466	400	83.9	148	591	435	142.0	212	852	537	449	231.7
86	469	400	85.8	150	609	437	148.8	214	852	533	449	231.7
88	474	402	88.8	152	597	437	144.3	216	851	530	449	231.3
90	474	402	88.8	154	607	439	148.1	218	844	528	449	229.0
92	479	402	91.7	156	613	443	150.3	220	852	528	444	231.7
94	481	402	92.8	158	624	444	154.3	222	859	543	449	234.0
96	489	406	97.2	160	613	446	150.3	224	851	539	449	231.3
98	487	405	96.1	162	633	448	157.6	226	851	543	449	231.3
100	493	406	99.3	164	624	448	154.3	228	852	533	449	231.7
102	500	407	102.9	166	641	449	160.4	230	852	551	454	231.7

[a] The calculated diameter (Cal. D) of Ag NCs is the required size of the particle number of Ag-NC seeds (N_{Seeds}) based on the classical growth model. [b] The center position of SPR peaks of Ag NCs changes with size in their extinction spectra, including the dipolar peak (Dipo.), the quadrupolar peak (Quadru.) and the octupolar peak (Oct.). [c] The actual diameter (Act. D) is obtained from the ML predicted model of optical simulation and the dipolar peak position of extinction spectra of the as-prepared Ag NCs.

Table S9. Summarized data of RGB colors of Ag NCs with size control.

Size (nm)	Color (a.u.)			Size (nm)	Color (a.u.)			Size (nm)	Color (a.u.)		
	R	G	B		R	G	B		R	G	B
40	254	226	39	104	180	141	140	168	190	191	164
42	254	225	38	106	178	141	142	170	191	192	164
44	254	225	39	108	176	140	143	172	196	194	168
46	254	224	38	110	175	142	144	174	196	194	169
48	254	222	38	112	173	143	146	176	196	194	169
50	254	218	38	114	171	146	148	178	195	192	169
52	254	213	39	116	170	150	150	180	198	193	172
54	254	212	39	118	170	153	151	182	199	194	173
56	252	207	39	120	169	153	152	184	201	195	175
58	250	204	39	122	169	157	154	186	200	192	175
60	246	197	39	124	168	159	155	188	205	194	180
62	243	193	38	126	166	160	156	190	207	196	182
64	242	186	39	128	164	160	156	192	209	198	185
66	241	181	40	130	162	161	158	194	209	197	187
68	240	177	41	132	165	162	157	196	208	196	186
70	239	175	42	134	166	163	157	198	205	194	185
72	238	172	48	136	168	164	157	200	204	193	186
74	235	167	55	138	169	165	157	202	208	197	188
76	228	158	63	140	170	169	157	204	210	199	190
78	225	155	70	142	171	171	157	206	210	199	190
80	221	151	75	144	173	173	157	208	209	201	192
82	218	149	82	146	177	177	158	210	207	201	192
84	211	143	86	148	178	179	158	212	205	199	191
86	205	138	90	150	179	180	158	214	203	195	188
88	203	136	96	152	180	181	160	216	204	196	188
90	201	136	103	154	181	182	159	218	206	199	191
92	200	136	106	156	180	182	160	220	208	200	192
94	197	136	113	158	180	183	160	222	206	199	190
96	195	137	120	160	182	185	161	224	209	203	194
98	191	137	125	162	182	185	161	226	209	204	195
100	187	138	131	164	184	187	162	228	208	203	194
102	185	138	133	166	186	188	163	230	208	203	195

Table S10. Summarized ML models of Ag NCs based on size control.

Factor	Training Dataset	ML Algorithm	R^2	RMSE	MaxAE
N_{Seeds} (n)	384	Logistic Regression	0.996	/	/
		ML model: $(13824+1.1784*10^{16}/n)^{1/3}$		（$\approx 2.32*10^5 n^{-1/3}$）	
RGB (i + j + k)	96	SISSO	0.995	3.343	10.772
	ML model: $0.006[(cos(ln k)j^2k/i]+0.184[(cos j\text{-}sin i)/cos(j^{1/2})]-2260.229[cos(j/i)/(i ln i/j)]+321.426$				

Table S11. Summarized spectral results of Ag NCs synthesized in scale-up experiments.

No.	Volume (mL)	FWHM (nm)	Dipo. (nm)	No.	Volume (mL)	Dipo. (nm)	No.	Volume (mL)	Dipo. (nm)	No.	Volume (mL)	Dipo. (nm)
1	1	56	425	36	1	497	71	1	603	106	1	773
2	1	56	425	37	1	493	72	1	603	107	1	770
3	1	56	425	38	1	497	73	1	603	108	1	772
4	1	56	425	39	1	495	74	1	601	109	1	772
5	1	56	426	40	1	497	75	1	603	110	1	775
6	1	56	425	41	1	497	76	1	603	111	1	775
7	1	56	425	42	1	497	77	1	599	112	1	770
8	1	56	425	43	1	499	78	1	599	113	1	760
9	1	55	425	44	1	497	79	1	603	114	1	770
10	1	56	426	45	1	497	80	1	601	115	1	758
11	1	56	425	46	1	495	81	1	601	116	1	760
12	1	56	425	47	1	495	82	1	603	117	1	765
13	1	56	425	48	1	495	83	1	603	118	1	768
14	1	56	425	49	1	495	84	1	603	119	1	768
15	1	57	427	50	1	495	85	1	603	120	1	768
16	1	56	425	51	1	495	86	1	605	121	1	765
17	1	55	425	52	1	495	87	1	603	122	1	768
18	1	56	426	53	1	495	88	1	603	123	1	770
19	1	56	425	54	1	495	89	1	603	124	1	760
20	1	56	425	55	1	495	90	1	605	125	1	762
21	1	56	425	56	1	495	91	1	603	126	1	765
22	1	56	425	57	1	495	92	1	607	127	1	765
23	1	56	426	58	1	495	93	1	605	128	1	765
24	1	56	425	59	1	495	94	1	603	129	1	768
25	2	56	425	60	2	500	95	2	608	130	2	768
26	2	55	425	61	2	497	96	2	603	131	2	772
27	2	56	427	62	2	497	97	2	602	132	2	769
28	2	56	425	63	2	502	98	2	602	133	2	769
29	2	56	425	64	2	501	99	2	603	134	2	772
30	2	56	426	65	2	497	100	2	603	135	2	770
31	5	56	425	66	5	495	101	5	605	136	5	770
32	10	56	428	67	10	499	102	10	603	137	10	766
33	50	56	428	68	50	495	103	50	601	138	50	765
34	300	56	426	69	300	500	104	300	602	139	300	755
35	1000	56	425	70	1000	499	105	1000	599	140	1000	763

Table S12. Summarized data of controllable synthesis of NCs.

Material	Synthesis	Optimization	Number of Valid Samples	Size (nm)	Yield (%)	Reference
Ag NCs	Manual work	Single factor	<70	10-200	>99	[2]
	Manual work	Single factor	<50	30-150	/	[3]
	Manual work	Single factor	<80	23-300	>99	[4]
	Manual work	Single factor	<40	104-119	/	[5]
	Manual work	Single factor	<50	19-140	>99	[6]
	Manual work	Single factor	<30	16-31	~100	[1]
Au NCs	Automated microfluid	Double factors	160	9-22	>88	[7]
	Manual work	Single factor	<50	14-120	~100	[8]
Ag NCs	Robotic automation	Multiple factors	>1200	24-200	>99	This work

Table S13. Summarized data of the performance of various colorimetric sensors in Hg^{2+} detection.

Material	Size (nm)	Surface Ligand	Linear Range (μM)	Detection Limit (nM)	Reference
Paper-based Ag nanoparticles	6-12	PVP	0.2-5	50	[9]
Ag nanotriangles	30-40	TSC and PVP	0.01-50	4	[10]
Au nanoparticles	13	Dithioerythritol	0.1-5	24	[11]
Au nanoparticles stain hydrogels	30-50	L-cysteine	0.2-200	3.7	[12]
Hollow AuAg nanocages	45	PVP	0.03-35	10	[13]
Cu nanoclusters	3-5	Metallothionein	0.097-16	44	[14]
Hollow MnFeO oxides	150-200	Thioglycolic acid	0.1-15	20	[15]
Hollow C@MoS_2 nanotubes	100-150	L-cysteine	0.01-100	3	[16]
Ag NCs	50	TSC	0.01-40	3	This work
		PVP	0.01-80	8	
		GEL	0.1-200	35	

Table S14. Summarized data of actual determination of Hg^{2+} concentration by applying the established approaches.

No.	Sample	Actual Hg^{2+} (μM)	Detected Hg^{2+} (μM, n=3)	Recovery (%, n=3)	RSD (%, n=3)
1	TSC-Ag NCs	0.2	0.19±0.01	95.0	2.83
2		0.4	0.38±0.02	95.0	1.67
3		0.8	0.83±0.05	103.8	2.33
4		2	2.05±0.11	102.5	1.78
5		4	3.87±0.15	96.8	2.73
6		8	7.83±0.31	97.9	2.51
7		12	12.67±0.62	105.6	3.29
8		24	22.91±1.21	95.5	2.95
9	PVP-Ag NCs	0.3	0.31±0.02	103.3	2.98
10		0.6	0.58±0.04	96.7	2.67
11		3	2.93±0.19	97.7	2.33
12		6	5.89±0.42	98.2	1.93
13		15	15.33±1.01	102.2	2.51
14		30	31.08±1.98	103.6	3.17
15		50	48.57±2.51	97.1	3.06
16		70	68.33±3.03	97.6	2.75
17	GEL-Ag NCs	0.9	0.88±0.05	97.8	2.03
18		9	8.67±0.53	96.3	1.98
19		45	42.68±2.52	94.8	3.23
20		90	93.23±3.98	103.6	2.67
21		120	115.67±4.51	96.4	3.07
22		140	133.92±5.03	95.7	3.33
23		160	155.98±5.55	97.5	2.11
24		180	187.33±6.48	104.1	2.73

Table S15. Summarized data of existing state-of-the-art practices assisted by AI.

Material	High-throughput Study with AI					Reference
	Data Modeling	Automated Synthesis	*In Situ* Characterization	ML Optimization	Targeted Application	
Pharmaceuticals	/	✓	/	/	/	[17]
Proteins	/	✓	/	/	/	[18]
Thioquinazolinone	/	✓	✓	✓	/	[19]
Organic mixtures	/	✓	✓	✓	/	[20]
Organic cages	/	✓	✓	✓	/	[21]
Metal-organic frameworks	/	/	/	✓	✓	[22]
Perovskites	/	✓	✓	✓	✓	[23]
Perovskites	/	✓	✓	✓	/	[24]
Au NCs	/	✓	/	✓	/	[7]
Ag NCs	✓	✓	✓	✓	✓	This work

✓ The work is closely related to the development of AI-based methods, which mainly serve as the technical means and approaches for the high-throughput study of advanced materials.

Reference

[1] H. Li, H. Xia, D. Wang, X. Tao, Simple synthesis of monodisperse, quasi-spherical, citrate-stabilized silver nanocrystals in water, Langmuir 29 (2013) 5074–5079. https://doi.org/10.1021/la400214x.

[2] N.G. Bastus, F. Merkoci, J. Piella, V. Puntes, Synthesis of highly monodisperse citrate-stabilized silver nanoparticles of up to 200 nm: kinetic control and catalytic properties, Chem. Mater. 26 (2014) 2836–2846. https://doi.org/10.1021/cm500316k.

[3] Z. Chen, J.W. Chang, C. Balasanthiran, S.T. Milner, R.M. Rioux, Anisotropic growth of silver nanoparticles is kinetically controlled by polyvinylpyrrolidone binding, J. Am. Chem. Soc. 141 (2019) 4328–4337. https://doi.org/10.1021/jacs.8b11295.

[4] L. Xing, Y. Xiahou, P. Zhang, W. Du, H. Xia, Size control synthesis of monodisperse, quasi-spherical silver nanoparticles to realize surface-enhanced Raman scattering uniformity and reproducibility, ACS Appl. Mater. Interfaces 11 (2019) 17637–17646. https://doi.org/10.1021/acsami.9b02052.

[5] L. Zhang, Z. Huang, Y. Han, Z. Guo, X. Zhang, R. Xie, W. Yang, Histidine-directed formation of nearly monodispersed silver nanoflowers and their ultra-high peroxidase-like activity under physiological pH, Appl. Surf. Sci. 532 (2020) 147457. https://doi.org/10.1016/j.apsusc.2020.147457.

[6] X. Liu, Y. Yin, C. Gao, Size-tailored synthesis of silver quasi-nanospheres by kinetically controlled seeded growth, Langmuir 29 (2013) 10559–10565. https://doi.org/10.1021/la402147f.

[7] H. Tao, T. Wu, S. Kheiri, M. Aldeghi, A. Aspuru-Guzik, E. Kumacheva, Self-driving platform for metal nanoparticle synthesis: combining microfluidics and machine learning, Adv. Funct. Mater. 31 (2021) 2106725. https://doi.org/10.1002/adfm.202106725.

[8] W. Leng, P. Pati, P.J. Vikesland, Room temperature seed mediated growth of gold nanoparticles: mechanistic investigations and life cycle assesment, Environ. Sci.: Nano 2 (2015) 440–453. https://doi.org/10.1039/c5en00026b.

[9] Monisha, K. Shrivas, T. Kant, S. Patel, R. Devi, N.S. Dahariya, S. Pervez, M.K. Deb, M.K. Rai, J. Rai, Inkjet-printed paper-based colorimetric sensor coupled with smartphone for

determination of mercury (Hg^{2+}), J. Hazard. Mater. 414 (2021) 125440. https://doi.org/10.1016/j.jhazmat.2021.125440.

[10] A. Amirjani, D.F. Haghshenas, Facile and on−line colorimetric detection of Hg^{2+} based on localized surface plasmon resonance (LSPR) of Ag nanotriangles, Talanta 192 (2019) 418–423. https://doi.org/10.1016/j.talanta.2018.09.079.

[11] D. Huang, X. Liu, C. Lai, L. Qin, C. Zhang, H. Yi, G. Zeng, B. Li, R. Deng, S. Liu, Y. Zhang, Colorimetric determination of mercury(II) using gold nanoparticles and double ligand exchange, Microchim Acta 186 (2019) 31. https://doi.org/10.1007/s00604-018-3126-6.

[12] X.J. Du, Y. Chen, L.Y. Qin, H.Q. Luo, N.B. Li, B.L. Li, Plasmonic gold nanoparticles stain hydrogels for the portable and high-throughput monitoring of mercury ions, Environ. Sci. Technol. 56 (2022) 1041–1052. https://doi.org/10.1021/acs.est.1c07217.

[13] J.-K. Chen, S.-M. Zhao, J. Zhu, J.-J. Li, J.-W. Zhao, Colorimetric determination and recycling of Hg^{2+} based on etching-induced morphology transformation from hollow AuAg nanocages to nanoboxes, J. Alloys Compd. 828 (2020) 154392. https://doi.org/10.1016/j.jallcom.2020.154392.

[14] R. Liu, L. Zuo, X. Huang, S. Liu, G. Yang, S. Li, C. Lv, Colorimetric determination of lead(II) or mercury(II) based on target induced switching of the enzyme-like activity of metallothionein-stabilized copper nanoclusters, Microchim Acta 186 (2019) 250. https://doi.org/10.1007/s00604-019-3360-6.

[15] Z. Lu, Y. Dang, C. Dai, Y. Zhang, P. Zou, H. Du, Y. Zhang, M. Sun, H. Rao, Y. Wang, Hollow MnFeO oxide derived from MOF@MOF with multiple enzyme-like activities for multifunction colorimetric assay of biomolecules and Hg^{2+}, J. Hazard. Mater. 403 (2021) 123979. https://doi.org/10.1016/j.jhazmat.2020.123979.

[16] L. Feng, L. Zhang, Y. Gong, Z. Du, X. Chen, X. Qi, X. Zhang, G. Mao, H. Wang, Hollow C@MoS_2 nanotubes with Hg^{2+}-triggered oxidase-like catalysis: a colorimetric method for detection of Hg^{2+} ions in wastewater, Sens. Actuators B 361 (2022) 131725. https://doi.org/10.1016/j.snb.2022.131725.

[17] S. Steiner, J. Wolf, S. Glatzel, A. Andreou, G. Keenan, T. Hinkley, G. Aragon-Camarasa,

P.J. Kitson, D. Angelone, L. Cronin, Organic synthesis in a modular robotic system driven by a chemical programming language, Science 363 (2019) eaav2211. https://doi.org/10.1126/science.aav2211.

[18] N. Hartrampf, A. Saebi, M. Poskus, Z.P. Gates, A.J. Callahan, A.E. Cowfer, S. Hanna, S. Antilla, C.K. Schissel, A.J. Quartararo, X. Ye, A.J. Mijalis, M.D. Simon, A. Loas, S. Liu, C. Jessen, T.E. Nielsen, B.L. Pentelute, Synthesis of proteins by automated flow chemistry, Science 368 (2020) 980–987. https://doi.org/10.1126/science.abb2491.

[19] G.-N. Ahn, J.-H. Kang, H.-J. Lee, B.E. Park, M. Kwon, G.-S. Na, H. Kim, D.-H. Seo, D.-P. Kim, Exploring ultrafast flow chemistry by autonomous self-optimizing platform, Chem. Eng. J. 453 (2023) 139707. https://doi.org/10.1016/j.cej.2022.139707.

[20] J.M. Granda, L. Donina, V. Dragone, D.-L. Long, L. Cronin, Controlling an organic synthesis robot with machine learning to search for new reactivity, Nature 559 (2018) 377–381. https://doi.org/10.1038/s41586-018-0307-8.

[21] R.L. Greenaway, V. Santolini, M.J. Bennison, B.M. Alston, C.J. Pugh, M.A. Little, M. Miklitz, E.G.B. Eden-Rump, R. Clowes, A. Shakil, H.J. Cuthbertson, H. Armstrong, M.E. Briggs, K.E. Jelfs, A.I. Cooper, High-throughput discovery of organic cages and catenanes using computational screening fused with robotic synthesis, Nat. Commun. 9 (2018) 2849. https://doi.org/10.1038/s41467-018-05271-9.

[22] P. Chen, Z. Tang, Z. Zeng, X. Hu, L. Xiao, Y. Liu, X. Qian, C. Deng, R. Huang, J. Zhang, Y. Bi, R. Lin, Y. Zhou, H. Liao, D. Zhou, C. Wang, W. Lin, Machine-learning-guided morphology engineering of nanoscale metal-organic frameworks, Matter 2 (2020) 1651–1666. https://doi.org/10.1016/j.matt.2020.04.021.

[23] Y. Zhao, T. Heumueller, J. Zhang, J. Luo, O. Kasian, S. Langner, C. Kupfer, B. Liu, Y. Zhong, J. Elia, A. Osvet, J. Wu, C. Liu, Z. Wan, C. Jia, N. Li, J. Hauch, C.J. Brabec, A bilayer conducting polymer structure for planar perovskite solar cells with over 1,400 hours operational stability at elevated temperatures, Nat. Energy 7 (2021) 144–152. https://doi.org/10.1038/s41560-021-00953-z.

[24] K. Higgins, M. Ziatdinov, S.V. Kalinin, M. Ahmadi, High-throughput study of antisolvents on the stability of multicomponent metal halide perovskites through robotics-

based synthesis and machine learning approaches, J. Am. Chem. Soc. 143 (2021) 19945–19955. https://doi.org/10.1021/jacs.1c10045.